Hydrogen generation promoted by single-atom based thermochemical catalysts

Srinivas Gadipelli[1,2,*], Jian Guo[1], Juntao Li[2], Hanieh Akbari[3], Christopher A. Howard[3], Hong Zhang[1], Neal T. Skipper[3], Jerry Barker[4], Paul R. Shearing[2,5], and Dan J. L. Brett[2]

[1]College of Physics, Sichuan University, Chengdu 610064, China
[2]Department of Chemical Engineering, University College London, London WC1E 7JE, UK
[3]Department of Physics & Astronomy, University College London, London WC1E 6BT, UK
[4]Redoxion Limited, Paper Yard, 11A Quebec Way, Canada Water, London SE16 7LG, UK
[5]Department of Engineering Science, University of Oxford, Parks Road, Oxford OX1 3PJ, UK
*Email: s.gadipelli@ucl.ac.uk

Abstract

Supplying energy cleanly and affordably without damage to the environment is one of the most pressing problems society now faces. Hydrogen can enable a low-carbon or net-zero emissions future; however, its generation on-demand and in mass quantities from thermodynamically stable gas, liquid and solid-state sources pose challenges, both environmentally and economically. Numerous catalytic routes have been proposed to promote H_2 production efficiently, and significant recent improvements have been achieved by designing atomic-level catalysts. This review presents a comprehensive account of advancements achieved with current and potential future H_2 generation technologies by single-atom-based catalyst materials (SACs). Reactions considered include wide range of typical and advanced reforming, partial-oxidation and direct dehydrogenation of various forms of hydrogen containing substances. The relevant fundamental catalytic reaction mechanisms along with maximum achievable H_2 capacities, high-performing catalyst materials and structure-activity insights are highlighted. Further perspectives are provided on CO_2 emissions, techno-economics, environmental impact, low-carbon and waste-based production, CO_2 capture and CO_x-elimination/H_2 purification.

Key words

Hydrogen generation; Single-atom catalysts; Catalysis; Reforming; Dehydrogenation; Cracking.

Introduction

To date, the most common sources of energy derive from burning non-renewable fossil fuels, including coal, natural gas and petroleum oil (eq.(1)-(2)). These processes release emissions into the atmosphere that pose serious risks to our planet, such as global warming, and are harmful and carcinogenic[1-6]. Therefore, a transition to net-zero emissions energy is essential[2]. This demands rapid development of new, renewables-based clean energy solutions. For example, hydrogen is earth-abundant and produces the highest energy density, 120 MJ $kg^{-1}{}_{H2}$, compared to any fossil fuel while carbon neutral (eq.(1)-(3))[7]. The global annual hydrogen demand is expected to grow considerably to 660 million tons by 2050 potentially accounting for 22% of global energy demand resulting in a reduction of 80 billion tons of CO_2 emissions , or 11% of the carbon reduction required for net-zero. Therefore, H_2-based energy systems are considered as one of the main pillars for realising net-zero global energy system[8,9]. However, terrestrial hydrogen is locked in water, hydrocarbon/organic matter, and requires energy-efficient extraction methods. Therefore, various catalytic routes have been proposed and developed to enable reactions under significantly reduced energy input.

$$C + O_2 \rightarrow CO_2\ (\Delta H = -394\ kJ\ mol^{-1} = -32.8\ MJ\ kg^{-1}; CO_2 =\ 3.67\ kg\ kg^{-1}) \ldots\ldots\ (1)$$

$$CH_4 + 2O_2 \rightarrow CO_2 + 2H_2O\ (\Delta H = -802\ kJ\ mol^{-1} = -50\ MJ\ kg^{-1}; CO_2 = 2.75\ kg\ kg^{-1}) \ldots (2)$$

$$2H_2 + O_2 \leftrightarrow 2H_2O\ (\Delta H = -242\ kJ\ mol^{-1} = -121\ MJ\ kg^{-1}) \ldots\ldots (3)$$

Catalysis: processes and catalyst materials

Fundamentally, bond-breaking of reactants and bond-forming of products are common features in catalytic conversion processes (eq.(1)-(3)). The catalytic process is usually governed by selective and functional catalyst nanostructure design[10-22]. Commonly used catalysts are solid heterogeneous materials, and catalysis reactions proceed on the surface of the catalyst. A particle size reduction of catalytic metal centres ($M_{subscript}$) from larger nanoparticles to ultrafine dispersion in the form of sub-nanometre atomic-clusters and ultimately single-atom centres (denoted as M_{NP}, M_{AC}, M_1, respectively) on suitable support structures have recently shown significantly enhanced performances, as depicted in **Fig. 1**[22-29]. Compared to nanoparticle catalysts (NPCs), single-atom catalysts (SACs) and atomic cluster or single-cluster catalysts (ACCs/SCCs) have shown enhanced mass and atomic efficiencies, along with conversion and production rates, selectivities and durabilities significantly[10-52]. Since heterogeneous catalytic reactions proceed on the surface of the catalysts, hose with enhanced surface area, which is exponentially increased by particle size reduction, enables adsorption and activation of reactants (**Fig. 1a-c**). Recent reviews elaborate the various forms of SACs to SCCs relevant structural diversity and developments[22,25].

H_2 production: current, under-developed and future potential routes

According to the international energy agency (IEA)[53], global H_2 demand reached ~100 million tons (or Mt) in 2023, of which <1% was produced at low-emissions. Around95% of H_2 currently in use was derived from steam reforming methane (SRM, eq. (4)),water-gas shift (WGS, eq. (5)) reactions, along with coal gasification, and biogas and oil/tar/naphtha reforming (**Supplementary note 1**). As a result, ~920 million tons of CO_2 was emitted, given emissions of 10-13 and 22-26 kg kg^{-1}_{H2} via SRM and coal gasification, respectively[53]. Understandably, SRM-WGS (eq.(4)-(5); $CH_4 + 2H_2O \rightarrow CO_2 + 4H_2, \Delta H = 165\ kJ\ mol^{-1}$) on equilibrium conversion results in CO_2 of ~5.5 kg kg^{-1}_{H2} and is a strongly endothermic reaction, requiring temperatures of 700-1000 °C (the heat provided by fossil fuels further contributes CO_2 to 5-7 kg kg^{-1}_{H2}). Notably, typical electricity powered water electrolysis H_2 production amounts CO_2 emissions to 24 kg kg^{-1}_{H2}. Therefore, there is urgency in advancing the low-emission and high-energy efficiency H_2 technologies. Aqueous-phase or steam reforming methanol (APRM/SRMe, eq.(6)) is emerging as a low-emission/energy-efficient route, due to relatively low-temperature(<350 °C) operation. Dry-reforming methane (DRM, eq.(7)), which uses CO_2 instead of steam and partial-oxidation of methane/methanol (POM/POMe, eq.(8)) with O_2 are other potential low-emission H_2 production routes. Ammonia dehydrogenation (ADH, eq.(9)) and methane pyrolysis (MP, eq.(10)) are inherently zero-emission reactions, and are potential low-carbon H_2 production technologies. Given their ultrahigh gravimetric/volumetric densities, the direct dehydrogenation of liquid organic hydrogen carriers (LOHCs, eq.(11)) and solid-hydrides (MgH_2, eq.(12)) have been long considered for potential on-board H_2 systems, which also offer combination of low-temperature and ultralow-emission merits relative to SRM or any other H_2 productions. Despite such potential, their real-world/large-scale supplies are limited due to the relatively low H_2 production capabilities and rates compared to SRM.

As depicted in **Fig. 1**, nanostructured catalytic materials have shown considerable advancements. Here, it is worth pointing that the reaction rates for ADH and H_2 production from SRMe have increased

exponentially as Ru and/or Pt particle size is lowered to atomic species (**Fig. 1d,e**)[11,29]. This enhancement also suggests high utilization efficiency of the catalysts. Significantly enhanced low-temperature conversion and dehydrogenation rates (two-to-three orders of magnitude) have been reported with SACs compared to NPCs counterparts (**Fig. 1e,f**)[10-52]. SACs/SCCs offer considerable improvements in durable reactions over NPCs (e.g. **Fig. 1g**)[12,22,45,52]. Such characteristics have been linked to improvements in adsorption and activation of reactants and desorption of products along with modified reaction pathways and will be comprehensively discussed in this review.

$$CH_4 + H_2O \rightarrow CO + 3H_2\ (\Delta H = +206\ kJ\ mol^{-1}) \dots\dots (4)$$

$$CO + H_2O \rightarrow CO_2 + H_2\ (\Delta H = -41\ kJ\ mol^{-1}) \dots\dots (5)$$

$$CH_3OH + H_2O \rightarrow CO_2 + 3H_2\ (\Delta H = +49.5\ kJ\ mol^{-1}) \dots\dots (6)$$

$$CH_4 + CO_2 \rightarrow 2CO + 2H_2\ (\Delta H = +247\ kJ\ mol^{-1}) \dots\dots (7)$$

$$CH_4 + \frac{1}{2}O_2 \rightarrow CO + 2H_2\ (\Delta H = -35.6\ kJ\ mol^{-1}) \dots\dots (8)$$

$$2NH_3 \rightarrow N_2 + 3H_2\ (\Delta H = +45.9\ kJ\ mol^{-1}) \dots\dots (9)$$

$$CH_4 \rightarrow C_{solid\ powder} + 2H_2\ (\Delta H = +76\ kJ\ mol^{-1}) \dots\dots (10)$$

$$CH_3OH \rightarrow CO + 2H_2\ (\Delta H = 90.7\ kJ\ mol^{-1})\ or\ LOHCs \rightarrow H_2\ lean\ LOHCs + xH_2 \dots\dots (11)$$

$$MgH_2 \rightarrow Mg + H_2\ (\Delta H = -75\ kJ\ mol^{-1}) \dots\dots (12)$$

Hydrogen production via CO_x path

This section discusses reforming, oxidation and dehydrogenation reactions that concomitantly generate CO/CO_2 by-products, in substantial amounts, from the reactions itself (eq.(4)-(8)), which need specific downstream separation/purification, such as WGS, CO preferential oxidation (PROX) and CO_2 capture/recycling.

Steam reforming

SRM is a well-established commercial technology and offers efficiency of 65 to 75%, among the highest of current commercially available production methods, yielding a substantial amount of H_2 production capacity (HPC). At thermodynamic equilibrium SRM yields 17.6 wt% HPC (eq.(4)), and the reaction is strongly endothermic. Typical catalytic industrial optimum conditions are 3–26 bar pressure with steam-to-methane (carbon fuel) ratio (S:C) of >2:1 and 700-1000 °C (**Fig. 2a-c**)[54-56]. As shown in **Fig. 2a-b, the** reaction consists of multiple and sequential steps, including the activation of methane (C–H) and water (O–H) over the catalyst and the formation of CO*, CO_2*, OH*, C* and H* species, which can form by-products (**Supplementary note 1**) and often deactivates catalysts via coking and sintering[54,55,57-59]. Literature suggests higher S:C of >1:1 inhibits coking via oxidative removal, but high steam can oxidize or hydroxylate catalyst to deactivate or accelerate its sintering via Ostwald ripening[58,60].

Ni-based NPCs, the typically-used catalysts with moderate price, offer good activity but are quite susceptible to sintering and coking. Usually, 15-25 wt% Ni_{NP} are dispersed on oxide carriers, where, activity scales with the degree of metal dispersion and thus local metal-structure or metal-support interactions (MSI) play a crucial role. Improvements have been achieved by down-scaling and alloying

to modify the electronic structure of metal centres while maintaining strong MSIs and balancing coking-decoking rates (**Fig. 2e**)[22,60,61]. Enabling SRM at lower temperatures with prolonged catalyst stability from coking is a challenging but energy efficient and low-carbon pathway. Recent studies have shown that catalysts with redox (such as oxygen vacancy (O_V) and lattice oxygen (O_L) involved) species can promote low-temperature (LT) SRM via dual-catalytic roles played by M_1 and MSI. Accordingly, Ni_1/CeO_2 showed a CH_4 conversion rate of 132 mmol g^{-1} h^{-1} at 600 °C, which was 5 times higher than Ni_{NP}/CeO_2 (**Fig. 2f**)[62]. Compared to Ni, Rh nanostructures exhibit the highest SRM activity and stability; Duarte et al. described the dual roles of Rh_1 and Rh_{NP} to promote C–H activation (to H_2 and C*) and C* oxidation (to CO and H_2), respectively (**Fig. 2a**)[58]. In-situ/operando DRIFTS revealed restructuring of Rh_1 sites to a high Rh–O coordination number and CO-liganded Rh_{AC} along with formation/reduction of surface hydroxyl groups/Ce^{4+} cations in LT-SRM (**Fig. 2g**)[63].

APRM/SRMe (eq.(6)) proceeds at relatively lower temperatures, <400 °C, thus Pt-based catalysts are typically preferred for higher activity and selectivity over Ni (or Cu) particles, which induce unwanted coking and methane production while sintering[12,14,29,31,57,64]. The main reaction products of APRM/SRMe are H_2, CO or CO_2 (**Figure 2b-d**), and often CH_4 (from the hydrogenation of CH_x* species) or coke are formed. Redox-active M_1/CeO_2 have shown multi-fold performance enhancement, compared to their NPC counterparts, with efficient adsorption/activation of CH_3OH via interfacial, MSI, O_V and $M_1^{\delta+}$ species;[14] e.g. M_1 and neighbouring O_V enabled MDH and dissociative adsorption (**Fig. 2d**)[12,57,65,66]. Zhang et al. showed that dual-active sites of Pt_1 and frustrated Lewis pairs (FLPs) on CeO_2 cooperatively generate H_2 (199-1,103 h^{-1} at 135-165 °C) at a rate of 2 to 3 orders higher magnitude compared to NPCs[31]. The turnover frequency (TOF) scaled with surface Ce^{3+} concentration (FLP density) due to accelerated formation of OH* and CO* intermediates (**Fig. 2h**)[57]. Different reaction pathways were proposed including formaldehyde and formate for excellent LT-SRMe by utilising α-MoC and γ-Mo_2N supports with superior water dissociation abilities[12,29,64,67]. While Pt_1/α-MoC produced efficient average TOF of 18,046 h^{-1} (**Fig. 1e**)[29], Pt_1/γ-Mo_2N@La with inert La overlayers to partially shield the reactive/redundant support that is responsible for oxidation-deactivation, and Pt_1 migration exhibited prolonged stability (**Fig. 1g)** and exceptional performance, turnover number (TON) of 15,300,000 in 800 h (**Fig. 2e**)[12]. The notable performance was attributed to favourable CH_3OH and H_2O dissociation along with lower CO* affinity of substrates, active interfacial structure and $Pt_1^{\delta+}$ sites.

Other higher hydrocarbons, e.g. (bio)ethanol ($C_2H_5OH + 3H_2O \rightarrow 2CO_2 + 6H_2$; $\Delta H_{H2} = 58\ kJ\ mol^{-1}$), propane, etc. can be reformed; they offer either low HPCs or reactions proceed at relatively higher temperatures and/or involve numerous side products (**Supplementary notes 1-2**)[19,51,62]. Commonly-used catalysts are late transition metals (Ni and Cu) and precious metals (Ru, Rh and Pt) that activate C–C and C–H bonds, thus are often plagued by limited stability and high CO selectivity. Improvements have been demonstrated by SACs with redox-active and multifunctional interfacial structures, such as Ni_1/CeO_2, Pt_1-Ir_1/α-MoC and Rh-$Ni^{\delta-}$-O_{Vs}-Ti^{3+}) compared to typical NPCs[19,51,62,68]. Overall, the redox-capable interfacial active structures improved the reforming activity with high selectivity and durability at significantly reduced temperatures. Often metals with high C–H activation exhibit poor O–H dissociation capability and/or weak stabilization of OH* intermediates, leading to unsatisfactory activity and unavoidable CO generation[17]. **Table S1** summarises the various reforming catalytic conversions and production rates. Although, methanol (ethanol) system is a simpler, promising and energy-efficient given its mild reaction conditions with high HPC of ~12.0 wt%, the development of catalysts with high conversion, low CO selectivity and high stability remains an ongoing challenge[57,65].

Dry reforming and partial oxidation

DRM (eq.(7)) utilises CO_2 gas, thus this system is simpler than APRM/SRM since it avoids water/vapour and offers environmental advantages with less CO_2 emissions. Nevertheless, it is highly endothermic,

normally requiring temperatures of ~1000 °C and offers poor quality H_2 (6.67 wt% in equilibrium from 1:1 H_2:CO mole ratio; **Figure 3**). Ni_{NP} dispersed on metal-oxide supports are typically used catalysts and are limited by rapid deactivation via sintering and/or coking[69]. In the catalysis, CH_4 adsorbs and activates on Ni to either CH_3* and H* or C* and 4H*, with rate-determining step (RDS) of dissociative adsorption of CH_x* species (**Fig. 3b**)[45,46,70-72]. Here, C* subsequently oxidizes by O species of MSI to produce CO, and O_V, like in SRM. In a redox-mediated reaction pathway, O_V produced are in turn filled with O* species of activated CO_2* (**Fig. 5c**)[45,46]. Different reaction pathways were discussed, including formate and bidentate intermediates, where CH_x* reaction with O* of activated CO_2 forms formate or CO* reaction with CO_2* produces carbonate[73].

Ni_1, $Ni^{\delta+}$–$O^{(2-\xi)-}$ or Ni_{AC} confined/stabilized by redox-active, mesoporous, defect/O_V-rich oxide supports (e.g. CeO_2 and MFI zeolites, SiO_2) have shown high CH_4 and CO_2 dissociation activities by generating C* and O* over Ni_1 and O_V, respectively. Catalysts with high O_V concentration or Lewis acidity, which also enhances MSI[74], presented highly durable (e.g. >1200 h at 800 °C)[75] performance via balanced C–H activation and CH_x* oxidation while preventing sintering (**Fig. 3c-e**)[45,75-79]. Their LT-DRM activity suffered from oxidation or coking[78], however, it improved significantly by Pt_1–Ni_1 and Ru_1–Ni_1 or Ce^{3+}–O_V–$Rh^{\delta+}$ interfacial sites (~90% H_2 yield; TOF of ~270,000 h^{-1} at 560-600 °C)[80] due to facile O_V, and O_V- and O_L-assisted CO_2 and CH_4 dissociation under low-activation barriers[46,81,82]. O_L-assisted anti-coking CH_3O* species via Ni–O active centres were observed by operando DRIFTs[83].

POM (eq.(8)) is a more efficient method as it offers high HPC, 12.5 wt% with reaction at ≥700 °C, via selective catalysis to limit its full combustion (to H_2O and CO_2) or other oxygenated and coking reactions (**Fig. 3f**)[54,84,85]. Compared to NPCs, the redox-active SACs (e.g. Pt_1/ZrO_2 and Rh_1/TiO_2) have shown ~100% H_2 selectivity with high stability (**Fig. 3g**)[84,86,87] due to weak binding of intermediates, e.g. CH_3* and H* formed on Rh_1 and O^{α} via Rh_1–O^{α} enabled facile adsorption/activation. A combustion-reforming pathway ($CH_4 + 2O_2 \rightarrow CO_2 + 2H_2O$ followed by DRM and SRM) was proposed over Ni-based SAA, $NiMo/SiO_2$, with oxophilic sites to limit O_2 poisoning (**Fig. 3h**)[88]. Notably, POM is in direct competition with the complete combustion reaction, which is highly exothermic, therefore selective catalysts are required. Chemical looping can be applied with oxygen carrier catalysts (OCs); e.g. Ni–O–Ce redox interface facilitates POM, where reduced OCs is subsequently replenished with oxygen via O_L carrier, like the mechanisms in SRM[89].

Both DRM and POM operate under dry conditions (**Table S2**) by utilizing CO_2/O_2 but offers low H_2 to CO product/selectivity values than SRM. There are several possible side-reactions, including reverse WGS. Among the catalysts, materials enriched with O*/OH* species, the O_L/O_V-mediated redox mechanism has been shown to be efficient for both conversion and coke-oxidation like in SRM/SRMe; while concurrently enhancing the oxygen mobility and storage capability of catalysts improved the intrinsic adsorption and dissociation of the CH_4, H_2O, CO_2 and O_2. The O_L involved oxygen-assisted pathway can promote rate-limiting C–H dissociation over M_1 sites with enhanced oxygen mobility/storage capacity[90]. In-situ and operando spectroscopy identify the anti-coking role of hydroxyl groups ($CH_x^* + OH \rightarrow CO^* + H^*$). Therefore, factors like CO_2 adsorption and surface hydroxyl or oxygen-rich groups in catalyst can enable DRM activity[81,91-94]. However, redox supports can also enhance reverse WGS side-reaction to reduce H_2 selectivity[95,96].

Direct dehydrogenation

The direct dehydrogenation of simple LOHCs such as formic acid (FADH), methanol (eq.(11)) and ethanol can be highly efficient as this can avoid steam burden and dehydrogenate at relatively low temperature/small energy input. These systems can offer high volumetric/gravimetric HPCs of 47-99 g L^{-1} (4.4-12.5 wt%; e.g. 99 g L^{-1} and 12.5 wt% from MDH (**Fig. 4; Fig. S1**)[32-34,38,40,57,97-99]. The dehydrogenation pathways include step-wise, partial dehydrogenation to intermediate products, e.g. formaldehyde ($CH_3O^* \rightarrow CH_2O^* \rightarrow CH_2OO^* \rightarrow COO^* \rightarrow CO + 2H_2$) or unwanted dehydration (e.g.

$HCOOH \rightarrow CO + H_2O$ to $HCOOH \rightarrow CO_2 + H_2$), methanation ($CH_4$) and oxidation ($CO/CO_2$)[98]. Cu-based catalysts exhibited high activity, requiring temperature of over 300 °C, but are unstable due to Cu sintering[98], therefore these reactions often rely on Pt-, Pd-based catalysts (**Fig. 4b-d**)[99].

Chen et al. showed that redox-active M_1–O_V (–Ce^{3+}) sites can offer 40 and 800-fold higher CH_3OH conversion rates (12,500 h^{-1}) than Pt_{NP}(2.5 and 7 nm)/CeO_2 at 300 °C (**Fig. 1f and 4c**)[40]. This delivered a H_2 TOF of 25,000 h^{-1} and ~70% CH_3OH conversion[57]. Efficient MDH was attributed to dissociative adsorption of CH_3OH on CeO_2 following diffusion of CH_3O* onto Pt_1 sites for dehydrogenation with weakly bonded CO[100]. PGM-free M^+–O_V interfacial sites[98] and Ni-based Ni_{AC} or Ni_1–N–C structures have shown improved durability from coking related deactivation, which is significant in Ni_{NP} or Pd_{NP}/N–C catalysts[38,101]. Those SACs comprising M^+ with O_V (redox active or Lewis acid) and M_1–N_x sites with optimised electronegativity and *d*-band centre of M_1, that determines adsorption and activation of FA, have shown to promote FADH with moderate adsorption energy of HCOO* and H* intermediates[102-104]. For example, Pt_3M_1–N_3–C sites of defective-carbon framework offered FA conversion TOF_{Pt} of 2,232 h^{-1} at 115 °C via sequential dissociation FA under lower energy barriers (**Fig. 4e,f**)[105]. Furthermore, catalytic centres on amine-functionalised supports yielded considerably improved LT-FADH at 50-60 °C[106,107]. Here, it is worth stating that O_V species can serve as a Lewis acids acting as a proton scavenger to promote O–H cleavage, while M^+ accelerates C–H activation. The electron-rich amino groups act as Brønsted bases to facilitate FA binding and O–H dissociation[108].

High performing catalysts face a trade-off with durability due to oxidation induced deactivation. In these reactions, the catalysts with a facile O–H and C–H cleavage and moderate binding of CO or intermediate tend to enable efficient H_2 production under high conversion rates and mild temperatures (**Table S3**). Compared to methanol, FA is non-toxic and promising for portable applications with simple dehydrogenation route, at relatively low temperature of ~100 °C compared to MDH. Ethanol dehydrogenation (EDH) occurs at high temperature, ~600 °C, with limited HPCs ($CH_3CH_2OH \rightarrow CH_3CHO + H_2$) compared to HPCs at their full dehydrogenation, which is more energetic and involving coking and $CO/CO_2/CH_4$ emission side-reactions ($CH_3CH_2OH \rightarrow CO + CH_4 + H_2$) and/or with low conversion under low-temperature[19]. PGM based SAA catalysts have shown improved activities/selectivities over NPCs[109].

Hydrogen production via CO_x-free path

A CO_x-free path H_2 generation (eq.(9)-(12)) not only produces high-pure H_2 but also eliminates CO/CO_2 purification (and coking/coke oxidation) steps altogether. This can ultimately result in significantly reduced carbon emissions or low-carbon H_2 production from the various extraction processes, such as methane and ammonia cracking and dehydrogenation of LOHCs and solid hydrides or from solid-state organic matter.

Methane pyrolysis

Methane pyrolysis (MP) splits CH_4 directly into H_2 and solid C and offers high-purity H_2 with highest HPC, 25 wt% (eq.(10)), among any H_2 delivery system. MP also offers high energy efficiency, >60%, while reducing CO_2 emissions to 4.37 kg $kg^{-1}{}_{H2}$[110]. The MP reaction enthalpy is comparable to SRM (37.7 vs 41.4 kJ $mol^{-1}{}_{H2}$). Practically, it remains challenging due to the strong C−H bond strength (434 kJ mol^{-1}) and high endothermic reaction (**Fig. 5a,b**)[54,55,111]. Typical transition metals-based NPCs (mainly Ni, Co and Fe; as their partially filled 3d-orbitals accept electrons from C–H bonds), facilitate CH_4 decomposition with low-apparent activation energy (E_a of 65 to 96 kJ mol^{-1}) under low-temperature. Yet, this suffers from low conversion/production rates with rapid catalysts deactivation due to severe coking and aromatic fouling as well as particle sintering as reaction proceeds via sequential adsorptive or dissociative pathways (**Fig. 5c**)[110].

Progress has been demonstrated via numerous catalysts/routes[110-114]. Yu and co-workers applied ball-milling assisted mechanothermal catalysis; Ir/Ni, Pt/Ni and Re/Ni SAA constructed on Ni balls showed steady-state CH_4 conversion (~5.8-14%) with H_2 yield of >10 g g^{-1} h^{-1} (~99.9% selectivity) and TOF of 1530 h^{-1} at 450 °C during 350 h. The reaction under vibration facilitates facile coke removal as static condition resulted in rapid catalyst deactivation with low-conversion rates (**Fig. 5c**)[113,114]. Machine learning predicted optimal SAA choice of Co, Ru, Re, Os and Ir loaded Ni with respect to the C–H dissociation energy barriers[114]. An overview of the catalysts and conditions with relevant CH_4 conversion and H_2 production/selectivity values is given in **Table S4**. The feasibility of pyrolysis heavily relies on the catalyst stability, and to mitigate this, plasma, molten-metal, fluidized and fixed bed reactors have been developed. For example, molten-Ni catalysts in bubble column reactors were durable as coke separates and floats on melt, yielding high H_2 rates (to 243 mL g_{Ni}^{-1} h^{-1}) with >95% CH_4 conversion at 800-1080 °C[111,115,116]. It was estimated that ~600 m^3 bubble reactor needed for 200,000 tons/annum H_2 plant, operating at 10 bar. The optimization of negative charge on Ni, or solute metal diffusivity that governs CH_3–H affinity and active site exposure/accessibility, respectively have been explored[117]. These systems can exhibit lower E_a of 81.2 kJ mol^{-1}, closer to the NPCs activity (**Fig. 5d**). Improved CH_4 conversion with increasing bubble-depth and controlling the bubble size via ballistic motion of bubbles at high-flow condition was reported[118]. Melt catalyst vaporisation along with ultrahigh-temperature requirement and low-methane conversion rates are the key limiting factors. Moreover, the oxidative reactivation of solid catalysts produces CO_x, a drawback of clean nature of MP.

Ammonia dehydrogenation

ADH offers high HPC, 17.6 wt%, under a mildly endothermic reaction (eq.(9)) that proceeds via step-wise dehydrogenation/dissociative adsorption (e.g. $NH_3 \rightarrow NH_2^* \rightarrow NH^* \rightarrow N^*$) followed by recombinative desorption[11,37,119-122]. The binding strength of N* is a descriptor for catalysts, which determines stability of N* and NH_x* intermediates. Notably, ADH benefits from the absence of coke/CO_x by-products, and from established global production/transportation for NH_3 that is liquefiable under mild conditions. Supported Ru_{NP} are extensively studied due to their moderate N* adsorption and high catalytic activity, however, this reaction requires >500 °C (**Fig. 5e,f**)(due to relatively slow kinetics and low NH_3 conversion, e.g. ~40% at <300 °C) and use of Ru limiting feasibility.

The electron-rich atomic levels of Ru or Ni centres in oxide-based catalysts, e.g. Ni/CeO_2 with Ni–O–Ce coordination formed via O_V and Ce^{3+} species, have shown promoted NH_3 activation and accelerated associative N*/N_2 desorption[37,120,122]. NH_3 coordination with Brønsted and Lewis acidic sites (electron-deficient metal centres is expected to increase N–H acidity) boosted –NH_2* and –NH* through sequential dehydrogenation. It was attributed that Ru_1 sites combined with proton-depleted O sites of Brønsted acids of support activate NH_3 synergistically via FLP ($Ru^{\delta+}$–$O^{\delta-}$) at low-kinetic barrier and H* migration to O-terminated oxide-support (**Fig. 5e**)[11,121]. This resulted in efficient NH_3 conversion of 4,100 h^{-1} at 450 °C (**Fig. 1d**)[11]. As shown in **Fig. 5g**, an order higher magnitude H_2 rate (594,000 mmol g_{Ru}^{-1} h^{-1}) was attained over Ru_{AC} compared to Ru_{NP}[37]. **Table S5** summarises the ADH activities with conversion/production rates, and suggests ≥450 °C is typical. Understandably, efficient and durable ADH can be achieved by electron-rich catalytic centres with redox-capable oxide supports that mitigate the reductive environment, which often causes catalyst deactivation via particle sintering. The introduction of alkali metals, O_V, defects improved the Ru–O coordination and enhanced electron transfer ability of interfacial active sites with strong MSI to inhibit strong H* adsorption (e.g. Ru–H, which can influence the reaction kinetics) while promoting LT-ADH multi-fold to their NPC counterparts[50,123]. These results that efficient ADH over non-PGM catalysts can be attained by enhancing the charge density of metal centres to alleviate hydrogen poisoning and decrease NH* activation barrier[124].

LOHCs and solid hydrides dehydrogenation

Reversible liquid-to-liquid and solid-to-solid substances are of significant interest due to their exceptional CO_x-free HPCs (volumetric) with high density, safety, compactness and on-board storage/transport feasibility (**Fig. 6; Fig. S1**)[30,32-34,36,38,40,41,43,47,57,97,98,125-129]. LOHCs of aromatic/N-heterocycles, such as cyclohexane (CH; C_6H_{12}), methylcyclohexane (MCH; $CH_3C_6H_{11}$) and dodecahydro-*N*-ethylcarbazole (12H-NEC; $C_{14}H_{25}N$) have shown great promise. Likewise, MgH_2 and NH_3BH_3 (ammonia borane, AB) HPCs (7.66 and 19.6 wt%; 150 and 110 g L^{-1}, respectively) are far higher performing than the US Department of Energy (DoE) H_2 targets (**Fig. 6b**). However, due to their high thermal stability, both LOHCs and solid hydrides suffer from low dehydrogenation rates at desirable on-board conditions. High-temperature requirements (>100 or to >400 °C) or high dehydrogenation enthalpy and kinetic barriers (e.g. MgH_2 with ΔH and E_a of 76 and 160 kJ mol^{-1} (eq. (12))) and subsequent challenges in reversible hydrogenation, cyclic efficiency have been major bottleneck issues.

Dehydrogenation of LOHCs is usually promoted by PGM catalysts, often with Pt- and Pd-related nanostructures coordination with –OH or O_V in the metal-oxide/hydroxide supports. For example, Pd_{AC} with optimised Pd–Pd coordination catalysed a step-wise dehydrogenation of 12H-NEC with TOF of 14,112 h^{-1} at 170 °C, that rate was 7 times higher than Pd_{NP} (**Fig. 6c**)[33]. Studies demonstrated that Pd^{n+}–OH or appropriate $Pd^{\delta+}/Pd^0$ ratio interfacial sites can accelerate C–H cleavage while reducing intermediates adsorption/H_2 desorption barrier[20,21,126,130]. Interestingly, CH and MCH dehydrogenation activities have been reported over Pt_1, Pt_{AC} and Pt_{NP} (a Pt−Pt coordination-number-dependent) based catalysts[32,34]; the Pt_1-O_V was extremely active for both CH and MCH dehydrogenation, and H_2 TOF reached >32,000 h^{-1} (330 g g_{Pt}^{-1} h^{-1}) for 30% CH conversion at 350 °C (**Fig. 6d**)[32]. This TOF was 309 times higher than commercial Pt/Al_2O_3 and Pt/CeO_2, which showed no activity until 400 °C. This indicates that synergistic role played by support with redox Pt−Ce coupling and O_V, as noted in the earlier sections. Notably high Pt utilization, high selectivity (>99% H_2) and record-high H_2 rate (268,380 h^{-1} or 518,760 mmol g_{Pt}^{-1} h^{-1}, at 300-350 °C) and stability (>2000 h) of Pt (from coking) was achieved with Pt−Fe SAA/clusters as overcoatings on NPCs or Pt_{AC} encapsulated in zeolites during MCH dehydrogenation[52,125,131]. These stabilized Pt sites generate abundant under-coordinated metal sites for facile C–H activation, which is also facilitated by low-coordinated Ni_x sites[127,132].

A high destabilisation degree was observed in milled or nanoconfined MgH_2 with Ni_1-based SACs (e.g. Ni_1/TiO_2) due to accelerated electron transfer between Mg^{2+} and H^- via Ni_1 induced O_V species/Ni–O–Ti^{x+} centres along with multivalent Ti^{n+} intermediates (**Fig. 6e**)[47]. This not only reduced the dehydrogenation temperature and improved thermodynamics (<70 kJ mol^{-1} H_2), but also enhanced kinetics and cyclic reversibility by forming Ni_1-Mg SAA and via H_2 spillover (**Fig. 6f**)[128,129,133]. A direct thermal destabilization of AB is limited due to slow H_2 release kinetics with concomitant release of poisonous ammonia and B–N complexes[134]. Although, nanoconfined AB yielded pure H_2 with fast kinetics under reduced temperature, it suffered from low amounts of confinement and low levels of H_2 production[134,135]. Since AB bears both protic (N–H) and hydridic (B–H) hydrogens with superior stability in air/water, hydrolysis ($NH_3BH_3 + 2H_2O \rightarrow NH_4^+ + BO_2^- + 3H_2$; ~8.9 wt% H_2) has been widely explored, often with Pt catalysts under alkaline condition. Among the Pt-SACs with different supports, a Pt_1/Co_3O_4 catalyst readily generated H_2 at 73,200 h^{-1} (375,000 mmol g_{Pt}^{-1} h^{-1}) at 25 °C[41,136]. Efficient catalytic hydrolysis proceeds via moderate AB adsorption and activation B–H, N–H and O–H bonds, like previously discussed reforming mechanisms over M_1^+ sites[30,36,137]. Likewise, Pt–Pt coordination, metal-oxide supports with O_V sites or Pt_1M_1 dimers/SAA with overlayers exhibited improved Pt utilisation, delivering H_2 to 86,640-720,000 h^{-1} (**Fig. 6g**)[43,137-141]. Optimized H* adsorption also contributes to efficient H_2 release[137]. Likewise, those Pt-free SACs offered competitive H_2 rates, e.g. 470,000-894,000 mL g_{Co}^{-1} h^{-1}[ref. 142,143].

Under suitable catalysis, methanol/ethanol partial dehydrogenation yields valuable liquid products without typical CO_x but offer low quantities of H_2[19,39,109]. Hydrolysis and methanolysis of various chemical hydrides including Mg/MgH_2 have been explored but attained lower HPCs due to high hydride stability (**Supplementary note 3; Table S6**)[144-147]. **Table S6** summarises the catalytic performance of various systems. The poor dehydrogenation rates and selectivity values with temperatures of >100 °C or limited H_2 delivery are some of the factors hindering their practical potential[48,52,130,148]. Moreover, these substances present several limitations and/or pose environmental challenges with toxicity (e.g. benzene, and low boiling point CH), energetics/economics and recycling/efficiency. Although AB and Mg are abundant, Mg is highly reactive and vulnerable to oxidation – its poor system level H_2 production/rate and reversible cycle life are major setbacks limiting the real-world use[134,135,149,150].

Water-gas shift and preferential CO oxidation

As noted, over 98% of impure hydrogen comes from carbon-based resources. WGS is applied for downstream purification process to eliminate CO from syngas and can yield additional 4.3 wt% H_2 (eq.(5)) under exothermic reaction. This process is usually operated at ~300 °C, thus PGM and Au-nanocatalysts are widely considered. It was proposed that CO absorbs on the metal centres, support activates H_2O and metal-support interface and O_V promotes further reaction via either redox (dissociative H_2O* to H* and OH*, and OH* splitting to O* and H*) or associative (OH* + CO* to carboxyl or formate intermediate) pathway (**Fig. 7a**)[14,18,42,44,57,151-157]. Here, in both cases, the dissociation of H_2O is generally considered RDS and catalysts with favourable H_2O decomposition activity can promote WGS.

Substantial improvements have been demonstrated with SACs and SAA via dual-metal active site enabled redox/associative pathway by generating O_V and $M_1^{\delta+}$–O–MSI interfaces[14,18,42,44,57,152-158]. For example, Lin et al. obtained CO conversion rate of 43,000 mmol g_{Ir}^{-1} h^{-1} at 300 °C over Ir_1/FeO_x[44].(**Fig. 7c**). The redox activity path with $M^{\delta+}$–O_V interfacial sites was identified as follows; Ce^{4+}–OH species reduce to H_2, CO_2 and Ce^{3+}–O_V, which re-oxidises with H_2O to H_2 and Ce^{4+}–OH regeneration. Here, rates of Ce^{4+} reduction/Ce^{3+} re-oxidation were close to those of CO_2/H_2 formation[14,23,159]. A strong MSI contributed to weak CO adsorption on Pt sites[160,161]. Likewise, Au_1–$(OH)_x$, Pt_1–$(OH)_x$ and Pt_1–$O(OH)_x$ sites on oxide supports have offered high performance and stability at <200 °C[39,162-164]. M_1/α-MoC systems exhibited exceptional LT-WGS activities with ~100% CO conversion (**Fig. 7d**) by producing key OH* intermediates[29,35,165-168]. A high M_1 utilisation efficiency and TON of 4,300,000 was observed with the combined Pt_1–Pt_{AC}, via direct CO dissociation **(Fig. 7d,e),** and offered record high mass-specific performance that meets 2004 DOE technical targets[35,167]. Cu, Co and Ni are PGM-free active metals[169]. The redox capable Co_1 and Ni_1 sites improved CO conversions and selectivities, over typical Ni_{NP}, which favours CO methanation[170].

Achieving WGS at relatively low-temperatures is desirable. Moreover, simple, efficient oxidation methods are required, e.g. preferential oxidation (PROX, eq.(13)) of CO in H_2 (**Fig. 7b**). However, typical catalysts face challenges to selectively oxidise CO with the competing H_2 oxidation/hydrogenation reactions (eq.(14))[171,172].

$$2CO + O_2 + H_2 \rightarrow 2CO_2 + H_2 \ (\Delta H_0 = -285\ kJ\ mol^{-1}) \ldots\ldots (13)$$

$$CO + 3H_2 \rightarrow CH_4 + H_2O \ (\Delta H_0 = -201\ kJ\ mol^{-1}) \ldots\ldots (14)$$

Advanced nanostructures, e.g. SACs-based $Pt_1^{\delta+}$ sites or Pt_1/FeO_x catalyst exhibited stable PROX performance at 80 °C as desirable than Pt-NPC via enhanced MSI with redox shuttle connected by labile oxygen[28,172-177]. Combined $Pt^{\delta+}$–$(OH)_x$–Fe^{3+} interfacial sites in synergy offered exceptional CO-

PROX (9,090 mmol g_{Pt}^{-1} h^{-1} at 25 °C) in a wide temperature window (25-225 °C) via $Pt^{\delta+}$–OH and Fe^{2+} sites facilitated carboxylate intermediate formation and O_2 activation, respectively[178]. Bimetallic sites combined with multi-metal/reduced oxide supports were explored for LT PROX (**Fig. 7f-i**)[172,179-183]. A closed loop mechanism ($H_2 + O_2 \rightarrow 2OH$; $2CO + 2OH \rightarrow 2CO_2 + H_2$) was proposed to accelerate CO oxidation, with OH groups as active intermediates, formed from dissociative H_2 activation/spillover[180]. In the process, a reversible oxidation, Fe^{2+} to Fe^{3+} by forming $Fe_1(OH)_3$ and COOH* and $Fe_1(OH)_2$ was observed, where irreversible Fe^{2+} oxidation leads to catalyst deactivation[181,182].

Other H_2 separation involves adsorption, e.g. porous or solvent to capture CO/CO_2, NH_3 and hydrocarbons), pressure-swing adsorption (PSA) for residual gas extraction, methanation of trace CO_x and membrane sieving or cryogenic distillation (e.g. CO_2, NH_3). Cu-based catalysts achieved highly selective hydrogenation from crude hydrogen (H_2+CO) feed to separate out CO[15,184]. There are several pathways proposed for CO_2 capture and conversion/separation and storage[185-192]. CO_2 capture via liquid amines is a well know technology and porous and solid-amine-based sorbents have advancing the performance[190,191,193]. Ni-based CO_2 reduction ($CH_4 + 2.9CO_2 \rightarrow 3.9CO + 0.1H_2 + 1.9H_2O$ ($\Delta H_{773\,K} = 113.6\ kJ\ mol_{CO2}^{-1}$)) was proposed to be energy efficient for scale[194].

Conclusions and perspectives

Hydrogen, with its non-polluting energy generation/storage potential, is a future pivotal substance for carbon-neutral technologies. Global hydrogen demand is expected to grow substantially; it is estimated that net-zero emissions require conversion of 85% of current fossil energy to H_2 and for that about 10 billion tons H_2 needs to be produced[195], which is two orders higher magnitude the 100 million tons demand in 2023. However, its viability critically depends on the energy, economics of its production alongside the assocaited carbon footprint/environmental impact. As detailed in this review, many projected methods rely on the deployment of efficient catalytic materials. Each have certain advantages and shortcomings..Conventional H_2 generators, while highly efficient, are huge CO_2 emitters; SRM offers high efficiency, about 65 to 75%, among the highest of commercial production rotues with several advantages, including high H_2 yield, reliable and low cost and supplies ~95% of current hydrogen demand. Its high-temperature operation contributes to significant CO/CO_2 by-products/emissions (e.g. >10 kg kg^{-1}_{H2})[196-199], which require subsequent purification/capture, and is not environmentally sustainable. DRM has been proposed for large-scale abatement of CO_2, but higher temperature operation, strong deactivating condition and low H_2 yield and low content in syngas makes it currently expensive and poses serious technical challenge for commercialisation[71,72]. Reforming of methanol has potential due to much lower operation temperatures and compact/on-board feasibility with high volumetric density (791 vs 0.657 g L^{-1} CH_4, i.e. 1200 times higher storage to CH_4), safe and efficient transportation. Associated CO_x by-products and low conversion/production rate factors are currently limiting the technology. Low-carbon/CO_x-free partial/controlled dehydrogenation, oxidation or reforming could be attractive, and is typically much faster than SRM and requires a smaller reactor but has lower H_2 yields.

Still in gas phase, but one-step processes, MP and ADH, are potential cleaner technologies due to their high and pure H_2 yields, not requiring CO_x purification/capture steps. However, they suffer from low conversion/production rates and life along with high temperature processes, which is a critical drawback for minimising net emissions . MP potentially achieves net carbon-negative output when using biogenic feedstock[200]. NH_3 offers more advantages as it is easily liquefied and offers high volumetric HPC of 121 g L^{-1}, a potential on-board H_2 store if H_2 rates can be improved under low temperature. Whereas, the direct dehydrogenation of LOHCs can release H_2 at relatively lower temperatures than CH_4/NH_3 and volumetric H_2 content (in the range 45-99 g L^{-1}) can meet the DoE H_2 targets. These systems can operate under simpler and more compact conditions, however, they suffer

from relatively low conversion/H_2 production rates, H_2/CO_x selectivities, requiring CO_x purification steps. The reversible liquid-to-liquid and solid-to-solid based H_2-rich-to-H_2-lean LOHCs and metal-hydrides with ultrahigh HPCs and high safety, are highly preferred technologies from CO_x-emissions/environmental point of view because of their low-carbon footprint, but they fall short of the DoE targets in terms of reversibility, kinetics and operating temperature[201].

The low-carbon, pure H_2 production or reduction of CO impurities/CO_2 emissions via either efficient catalytic H_2 production process or CO_x capture/separation is another important aspect for H_2 to be carbon neutral energy. Direct CH_4 pyrolysis, dehydrogenation of NH_3, LOHCs and solid hydrides are transformative CO_x-free H_2 production pathways with a significant scope of storing/generating considerable amounts of H_2. High purity H_2 is required for numerous hydrogenation/oxidation reactions including re-hydrogenation and/or synthesis of LOHCs and NH_3, and H_2 fuel cells[171]. As discussed, WGS and CO PROX under low-temperature is promising. Hydrogenation reactions were successfully attained from crude hydrogen feed containing high amounts of CO, for which catalysts showed no activity, thus pure CO was collected in the tail gas[15,184]. CO_2 can be easily separated by cryogenic distillation compared to CO. WGS can contribute to H_2 production and is crucial for utilizing alternative bio/waste based sustainable feedstocks. H_2 purification from trace CO levels via CO-PROX can be viable approach among PSA, membrane separation and hydrogenation/methanation. Efficient CO_2 separation/sequestration capabilities have been reported via adsorption/separation and conversions with porous and amine structures[194,202,203].

The most commonly used catalysts for CH_4 derived H_2 via SRM, DRM and MP are Ni based, because of its low cost and good activity; however, Ni_x is quite susceptible to sintering and coking. The highest SRM activity and superior deactivation suppression, even at relatively high/low temperatures, can be achieved with Rh or Ru, but at a higher cost. Remaining H_2 production and purification are efficiently driven by PGM-based catalysts, as many of these are operated at mid or low temperatures for which Ni shows poor activity, for example, dehydrogenation of LOHCs, NH_3 and Abor MgH_2 are often enabled by Pt, Pd and Ru centres. Catalyst metal centres are usually supported on oxide carriers to maximise the dispersion as their activity scales with the dispersion, which further indicates that the local metal structure is important[204,205].

In SACs and ACCs, the positively charged atomic centres with strong MSI exhibited high performances. M_1 centres usually exhibit high oxidation states rather than metallic states owing to the coordination with non-metal atoms in the supports. Considerably prolonged stabilities are observed in atomic level catalysts while inhibiting/resisting from typical coke, CO, oxidation, hydroxylation, temperature or other relevant catalyst deactivation sources. These systems are capable of ≈100% exposure of M_1 sites, facilitating exceptional atomic utilisation efficiencies/specific activities to deliver multiple-to-few orders magnitude increase in the conversion/production rates and selectivities at significantly reduced temperatures. There is a common catalytic reaction mechanism for most of the H_2 generation methods; reducible oxides supported SACs or redox-active support (e.g. CeO_x)-based SACs are typical high-performing structures for almost all the H_2 generation reactions discussed. Relevant catalyst materials design and structure-performance insights on various catalysis reactions have been further discussed in a recent article[22].

Considering techno-economics, of low-carbon, efficient processes, SRM can be feasible with carbon capture and sequestration (CCS) technology; with 85% CO_2 capture contributing to considerable emission drop down to ~2 kg kg^{-1}_{H2}. SRM-CCS estimated to reduce the energy efficiency (from 75 to 60%) that translates to a >30% increase in H_2 cost. According to the IEA, a number of factors influencing the uptake of CCS with high cost/low efficiency has been the major limiting factor[206]. DoE set H_2 the production cost target at US$2 kg^{-1}, equivalent to a gallon of gasoline based on similar energy content, for various reforming/gasification routes[196,197]. This cost is a reference to assess the feasibility of new

hydrogen production methods, and an acceptable cost for a net-zero emission scenario by 2050 was suggested to be about US$(1–2) kg^{-1}_{H2}. SRM stands out given its high efficiency and low production (US$1.25-3.50 kg^{-1}_{H2}) cost among other H_2 productions of pyrolysis, gasification and renewable liquid (methanol, ethanol, glycerol) reforming, and other clean photobiolysis or water electrolysis [198].

Currently, DRM is undesirable for large scale H_2 production, but has the potential to be more efficient with high performance SACs based LT operations. Whereas, MP can be cleaner (CO_2 emission reduction of 4.37 kg kg^{-1}_{H2}), competitive to SRM (comparable enthalpy, 37.7 vs 41.4 kJ mol^{-1}_{H2}), and the energy efficiency of MP (58%) can match the SRM-CCS system[110]. Here, it is worth noting that thermodynamically, MP requires 7 times less energy than H_2O splitting (37.7 vs 286 kJ mol^{-1}_{H2}) to produce the same amount of H_2, meaning that MP requires 13-26% of energy used in electrolysis, thus MP offers significant cost benefits. Industry including BASF, Shell and Monolith are advancing pilot-scale MP-H_2 production (turquoise hydrogen) with IEA rating it from three to eight on its technological readiness-level (TRL) – a score of nine inferring scaled commercial readiness[207]. The other clean H_2 technologies of NH_3, LOHCs and metal/chemical hydrides are currently too expensive or do not meet the production rates and/or capacities under viable conditions set by DoE[48,208-211]. The main advantages of these routes are that the catalysts are free from coke deposition and generate high-purity H_2, thus avoiding the need for down-stream purification. The target performance of ADH via Ru-based catalyst for on-site H_2 fuelling station required to exceed NH_3 conversion of 99.5% at 500 °C and 30,000 h^{-1}[ref.210]. The total energy efficiency of NH_3 and MCH is about 34-37 and 25%, respectively, while liquid hydrogen has 30-33%[211].

Moreover, SACs can make PGMs cost-effective and can be applied in future potential H_2 production routes that are strictly limited by the cost of PGMs, since SACs typically comprise about 1 wt% of metal compared to usual 20 wt% in conventional NPCs. This means that SACs can reduce the catalyst costs to more than an order of magnitude compared with NPCs. Their high catalytic efficiencies, along with exceptionally enhanced reaction rates under significantly reduced temperatures, further contribute to a considerable reduction in the PGMs costs, thus some of the potential, low-carbon methanol reforming/dehydrogenation, WGS, ADH, LOHCs and hydrides can emerge as viable. Likewise, those extensively-studied PGMs catalysts across a wide range of H_2 production routes, for which PGM-based bimetallics formed via a second transition metal (relatively low cast 3d or 4d block metals) have been shown to maximize catalytic activity and atom utilization, which makes PGMs even more affordable and durable[138,139,141,209,212].

Low-carbon H_2 production in small to large scale could be attained via integrated systems in synergy with controlled catalysis by utilising bio-based liquids and solids as well as waste substances, such as ethanol and plastics. SACs driven CO_x-free routes via self-coupling ($2CH_3OH \rightarrow HC(=O)O - CH_3 + 2H_2$) or partial-reforming ($C_2H_5OH + H_2O \rightarrow 2H_2 + CH_3COOH$, $\Delta H = +41.8$ kJ mol^{-1}) and partial-oxidation ($CH_3OH + \frac{1}{2}O_2 \rightarrow CO_2 + 2H_2$; 8.3 wt% H_2) can be simple and more effective[39,51,212,213]. Here, multifunctional interfacial structures, such as Pt_1-Ir_1/α-MoC, Rh-$Ni^{\delta-}$-O_{Vs}-Ti^{3+} or PGM_1/ZnO performance (90% H_2-CO_x selectivity and ~40% CH_3OH conversion) can be 2-3 orders of magnitude higher than NPCs, which favour C–C cleavage and CO_x selectivity[51,212,213]. Techno-economic analysis and life-cycle assessment of partial-reforming ethanol suggests its economic viability for an industry-scale plant[51]. Remarkably high stability (>2000 h) and catalyst regeneration over consecutive cycles during MCH-H_2 (>99.9% pure H_2) could be feasible with bimetallic PtFe clusters or PtCo SAA, which showed high Pt utilization efficiency and mass-specific activity to 51 and 23 fold higher than NPCs[48,52]. Likewise, 12H-NEC dehydrogenation with low enthalpy, 50.6 kJ mol^{-1}, and low-cost MCH-toluene cycle with impressive volumetric H_2 density of 56 g L^{-1} (~600 L L^{-1}_{MCH}) is attractive, the large-scale H_2 release cycles relies on the catalyst.

Upcyling biomass and plastic waste - renewable raw material - to H_2 is feasible under advanced catalysis. Waste plastics (wP, such as milk containers/plastic bags (polyethylene (PE), $(C_2H_4)_n$, food wraps (polypropylene $(C_3H_6)_n$) and plastic foam (polystyrene $(C_8H_8)_n$)) comprise high H/C ratio and low O/C ratio than biomass (CH_4 and CO_2 content in biogas ranges 50-70 and 35-45%, respectively). Biomass derived acetic acid (HAc), lignocellulose, bio-oil, glycerol offers great opportunity for H_2 generation[214-220]. The conventional biomass-H_2O gasification and steam reforming is troubled by significant amounts of CO_2 and tar products, while highly energy-intensive (e.g. $Seaweed + H_2O \rightarrow H_2 + CO + CO_2 + CH_4 + CH_x + Tar + Char$)[220]. Hydrogen utilization efficiency of 67.8% at 550 °C was achieved from steam reforming of bio-ethanol[68]. Typically used catalysts are Ni_x nanocatalysts[216,218,221]. Autothermal reforming HAc (with 2.64 mole-H_2 per mole-HAc) presented higher energy efficiency and economic viability[222]. Alkaline substances, NaOH, CaO, etc. were introduced for simultaneous CO_2 sorption in-situ (via $CaO + CO_2 \rightarrow CaCO_3$) or to promote H_2; cellulose fragmentation in aqueous phase reforming: $C_6H_{10}O_5 + 12NaOH + H_2O \rightarrow 6Na_2CO_3 + 12H_2$, can generate high-purity H_2 while capturing CO_2 as carbonates[216,218]. Likewise, CO_2 recycling based biogas, ethanol and glycerol reformation, or bi-and tri-reforming of methane that combines DRM and SRM (and POM) reactions ($3CH_4 + CO_2 + 2H_2O \rightarrow 8H_2 + 4CO, \Delta H = 660\ kJ\ mol^{-1}$) as compact, efficient, low-coking H_2 processes have been reported[203,223,224].

Catalytically cracking wP into H_2 appeared promising; e.g. PE is abundant and has up to 14.4 wt% H_2 capability. Plastic decomposition or pyrolysis typically requires high temperatures and a multi-step process, leading to significant CO_2 emissions and low H_2 selectivity (theoretically <75 vol% under steam-reforming). Combining pyrolysis, steam reforming and WGS boosted the H_2 yields from plastics to 120 mmol $g^{-1}_{plastic}$ at 550 °C, over conventional thermal catalysis[225]. Significant progress has been reported via catalytic mechanochemical and microwave irradiation routes[217]. For example, ball milling PE at 45 °C achieved H_2 yield rate at least 3 orders of magnitude higher than thermocatalysis at 430 °C[49]. A performance of high H_2, 99.4 vol%, of 70.3 mmol g^{-1}_{PE} with exceptional H_2 recovery ratio of 98.5% was about 6 times greater than thermocatalysis; 11.2 mmol g^{-1}_{PE}, 15.7%), indicating a high-purity H_2 route with net-zero carbon emissions. Likewise, Fe-Co based catalysts under microwave irradiation facilitated a high H_2 yield of 56-61 mmol g^{-1}_{wP} with an efficiency of over 80–97 wt% H_2 by promoting C–H activation and deep-dehydrogenation of alkene/aromatic intermediates to solid-carbon[220]. Moreover, an environmental sustainability assessment suggested that H_2 production via wP gasification coupled CCS becomes cheaper compared to electrocatalysis while reducing the climate impact (net negative climate change impact of −371 kg CO_2 per tonne of mixed wP treated) caused by methane/hydrocarbon-based and most electrolytic H_2 generation methods[226,227].

In summary, thermocatalytic H_2 production routes coupled with atomic-level catalysts play a significant role in the energy sector in near and long-term due to slow uptake of other clean energy and electrocatalysis and photocatalysis based green hydrogen supply technologies[199,228-230], which are expensive and notably can be CO_2 intensive (e.g. typically 0.8-4.6 kg CO_2 kg^{-1}_{H2} but this can be much higher)[230,231]. A recent perspective report discussed the status of the hydrogen economy, and what is needed to deploy the hydrogen economy as part of the global drive towards a net-zero emission world[232].

Figure files

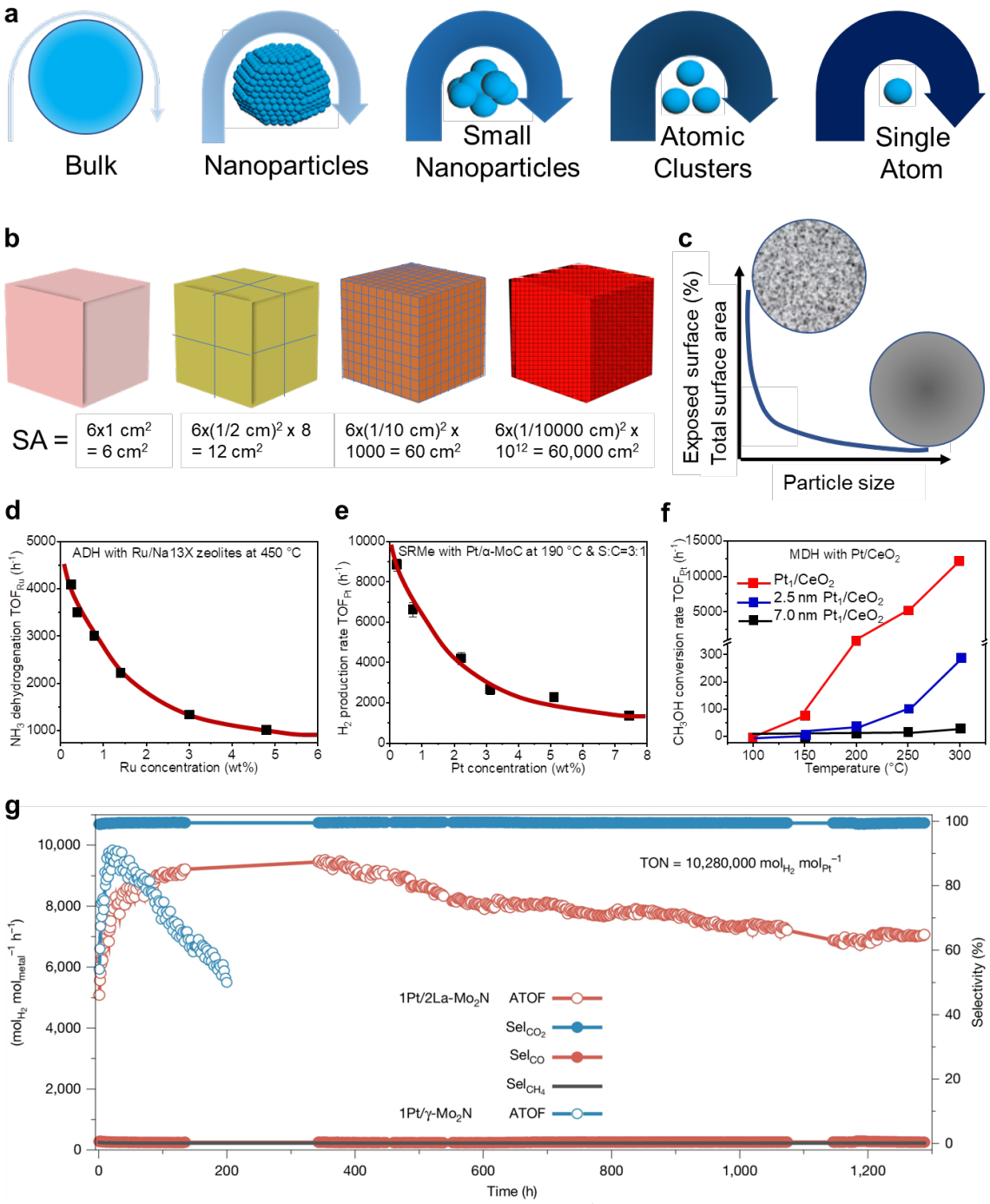

Fig. 1. Overview of catalysis and catalyst particle size driven activities. a) Catalytic conversion against catalyst particle size, from bulk to single-atom centres; increase in thickness of curved arrow represents improved conversion efficiencies. **b,c)** Particle size reduction results in exponential increase of surface. **d,e)** Catalytic activity trend against concentration of metal centres; TOF values of NH_3 decomposition over Ru/Na13X zeolites at 450 °C with 30,000 mL g_{cat}^{-1} h^{-1}[ref.11] (e) and H_2 rate of SRMe with Pt/α-MoC catalyst at 190 °C and S:1 = 3:1[29] (f). Here, with increasing metal loading leads to formation of nanoparticles and their size, which decreases catalyst efficiency exponentially with rapidly reduced TOFs. **f)** TOF of CH_3OH conversion in MDH over Pt/CeO_2 with respect to temperature showing rapidly enabled low-temperature activity with reduced Pt particle size from Pt_{NP} to Pt_{AC} to Pt_1[ref.40]. **g)** Catalytic activity of the 1Pt/γ-Mo_2N and 1Pt/2La-Mo_2N catalysts and selectivity of the 1Pt/2La-Mo_2N catalyst in the methanol-reforming reaction. Conditions: catalysts 150 mg, reaction temperature 200 °C, pressure 5 bar, methanol/water = 1/3 (molar ratio), weight-hourly space velocity ($WHSV_{methanol}$) = 12.87 h^{-1}[ref.12].

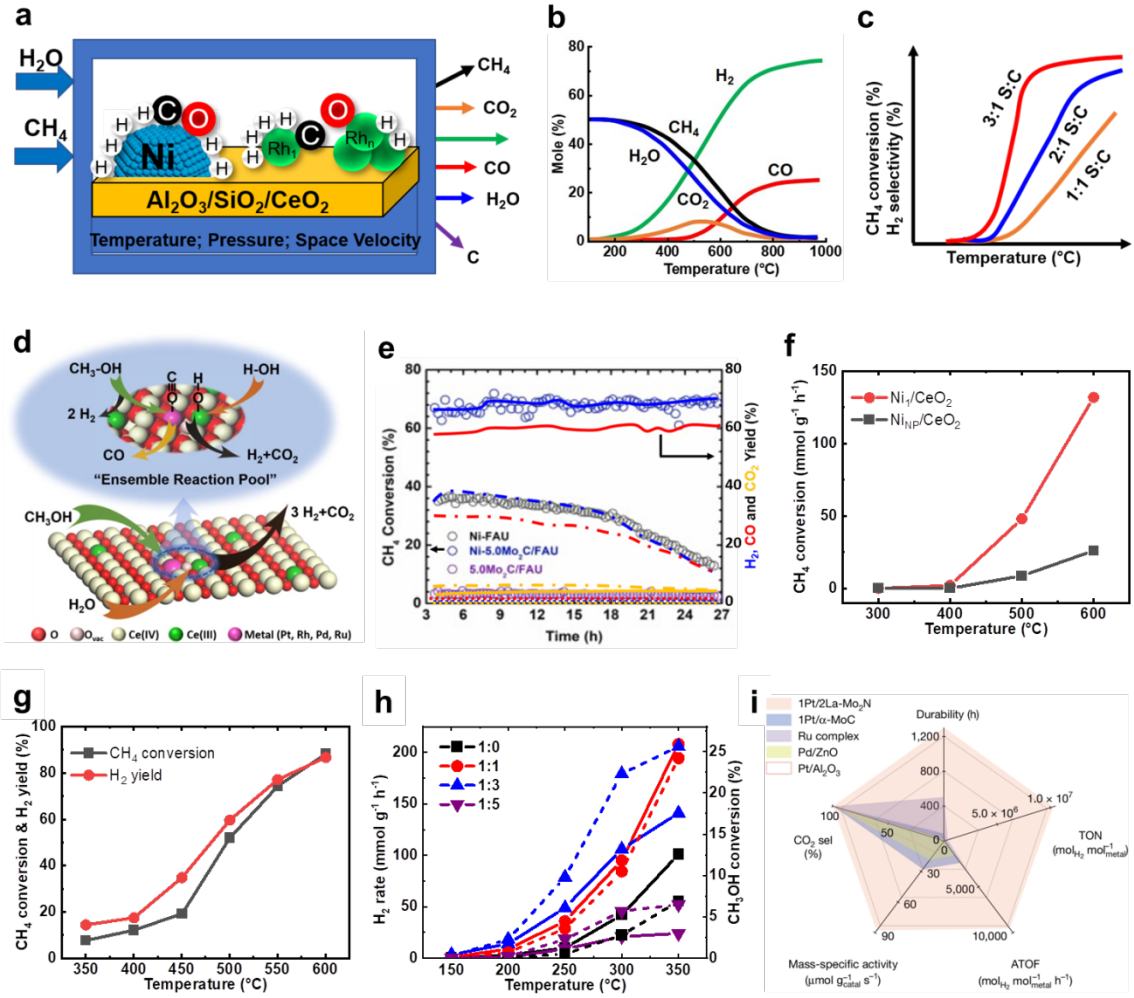

Fig. 2. Steam reforming mechanisms and SACs based activities. a-c) Schematic SRM reaction over NPCs and SACs[58]. (a); equilibrium curves at 1 bar and 1:1 mole S:C[55]. (b); CH_4 conversion and H_2 selectivity against S:C ratio and temperature (c). **d)** O_L and O_V mediated (SRM) SRMe pathway on M_1/CeO_2[ref.57]. **e)** CH_4 conversion (circle data), and H_2 (blue data) CO (red data) and CO_2 (yellow data) yields against temperature over Ni-SAC and NPC at 850 °C; 20 mg catalyst, 2% CH_4 and 16% H_2O at 100 mL min^{-1}[ref.60]. **f)** CH_4 conversion over Ni_1/CeO_2; 55 mg catalyst, CH_4 = 20.3 mL min^{-1}, H_2O:CH_4 = 1:1[62]. **g)** Rh_1/CeO_2 induced CH_4 conversion and H_2 yield against temperature; 50 mg catalyst, H_2O:CH_4 = 2:1 (10% CH_4 at 20 ml min^{-1})[63]. **h)** H_2 generation rate (solid-line data) and CH_3OH conversion (dashed-line data) against temperature over Ru_1/CeO_2 at different ratios of H_2O:CH_3OH[57]. **i)** Comparison of key catalytic performance in the SRMe over five dimensionalities (durability, TON, ATOF, mass-specific activity and CO_2 selectivity) for 1Pt/2La-Mo_2N, 1Pt/α-MoC, Ru complex, Pd/ZnO and Pt/Al_2O_3 catalysts[12].

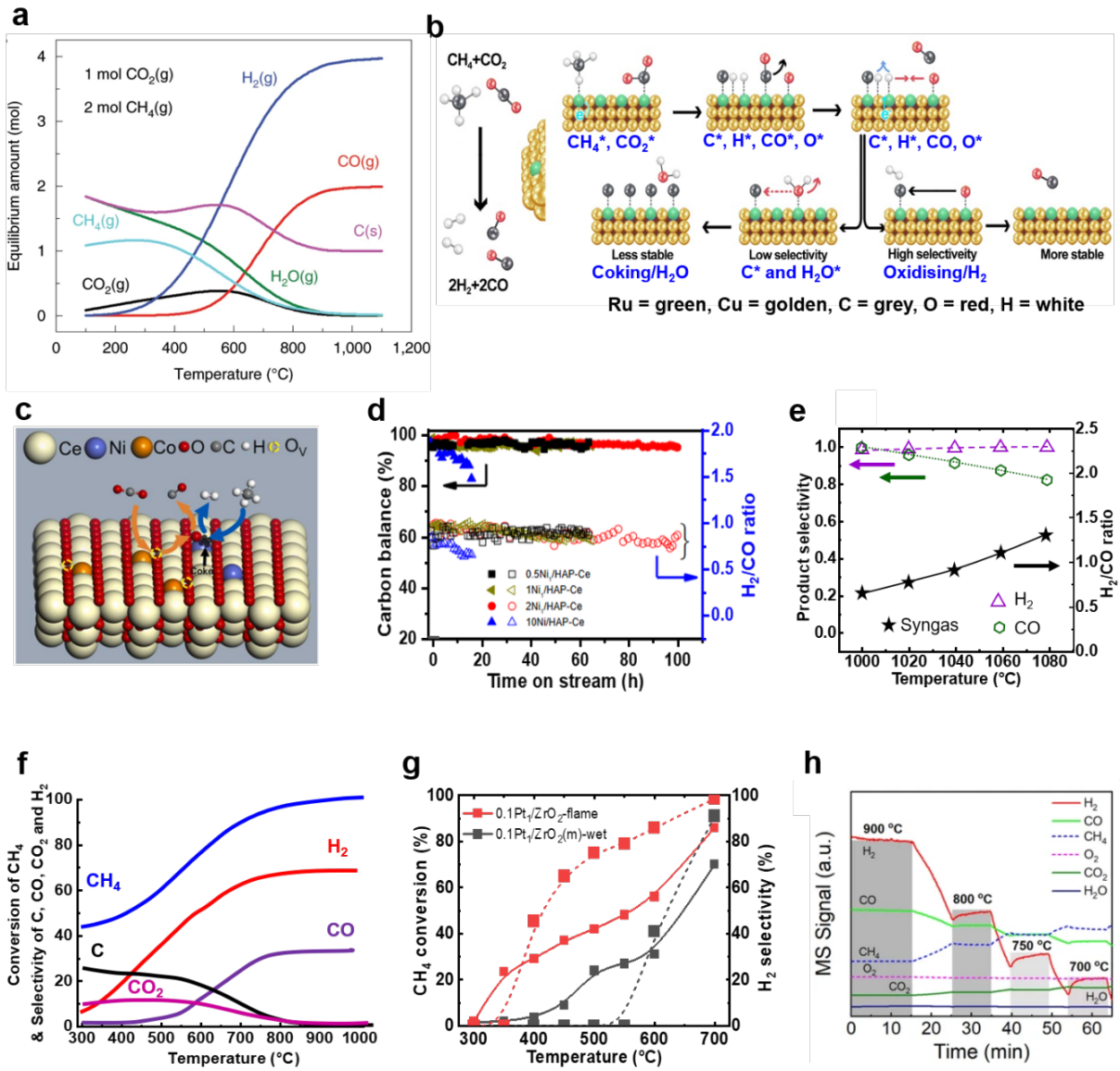

Fig. 3. DRM mechanism and activities of SACs. a) Thermodynamic equilibrium curves under 1 bar[72]. **b)** Schematic reaction mechanism and selectivity[70]. **c,d)** Catalyst lifetime test of $Ru_{1.5}/Ni_1$-MgO-R and $Ru_{1.5}$/MgO-R during DRM. Reaction conditions: catalyst = 50 mg, T = 800 °C, CH_4/CO_2/Ar = 1:1:8, gas flow = 50 mL min^{-1}, WHSV = 60 L g^{-1} h^{-1} [ref.75]. **e)** Carbon balance and H_2:CO selectivity over HAP-Ce supported Ni_1 and Ni_{NP} catalysts at 750 °C, CH_4/CO_2/He = 10/10/30, GHSV = 60,000 mL g^{-1} h^{-1}[ref.76]. **f)** POM equilibrium curves against temperature[54]. **g)** CH_4 conversion and H_2 selectivity over Pt_1/ZrO_2, under 30 mg catalyst, 3.33% CH_4 and 1.67% O_2 at 30 mL min^{-1}[ref.86]. **h)** Steady and transient state temperature-programmed surface reaction of CH_4 and O_2 coupled with mass spectra (TPSR-MS) experiment for AD MoNi alloy/SBA-15 under testing condition with CH_4:O_2 = 2:1 flow for identification of POM mechanism[88].

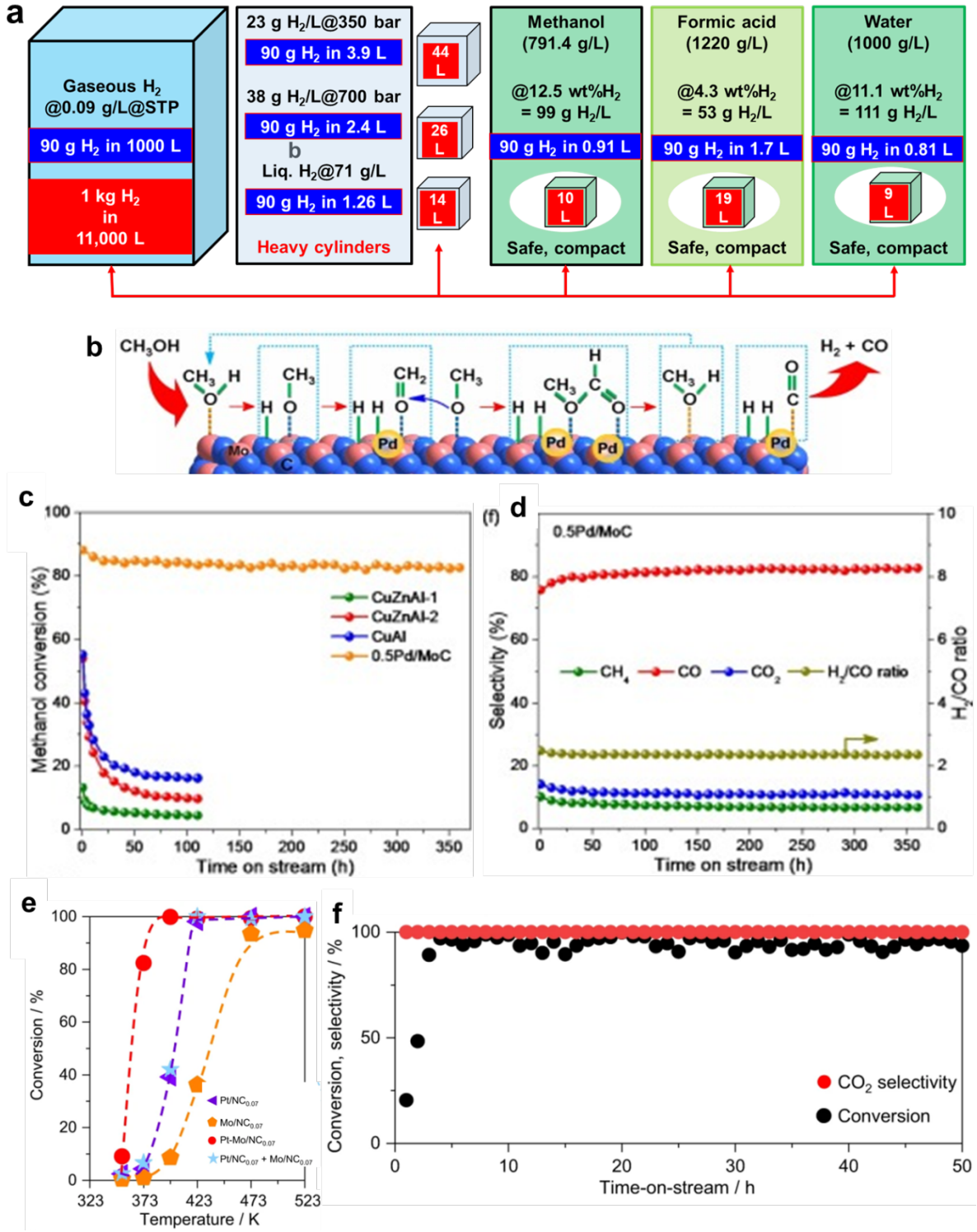

Fig. 4. Direct dehydrogenation of LOHCs. a) A comparative advantage of liquid H_2 stores with relevant mass and volume-based capacities compared to reference H_2 gas at STP and under highly compressed or liquefied conditions. **b)** Schematic MDH pathway over Pd/MoC[99]. **c,d)** Stability test for methanol decomposition performed on different catalysts at 240 °C: methanol conversion (c), H_2 production rate (d), product selectivity and H_2:CO ratio (e) under methanol flow rate, 0.6 mL h^{-1}; N_2 flow rate, 32.0 mL min^{-1}; catalyst loading, 230 mg at 160 °C and 1 bar[99]. **e,f)** FA conversion and CO_2 selectivity as a function of bed temperature (e) and long-term stability performance of Pt-Mo/$NC_{0.07}$ at 373 K (f)[105].

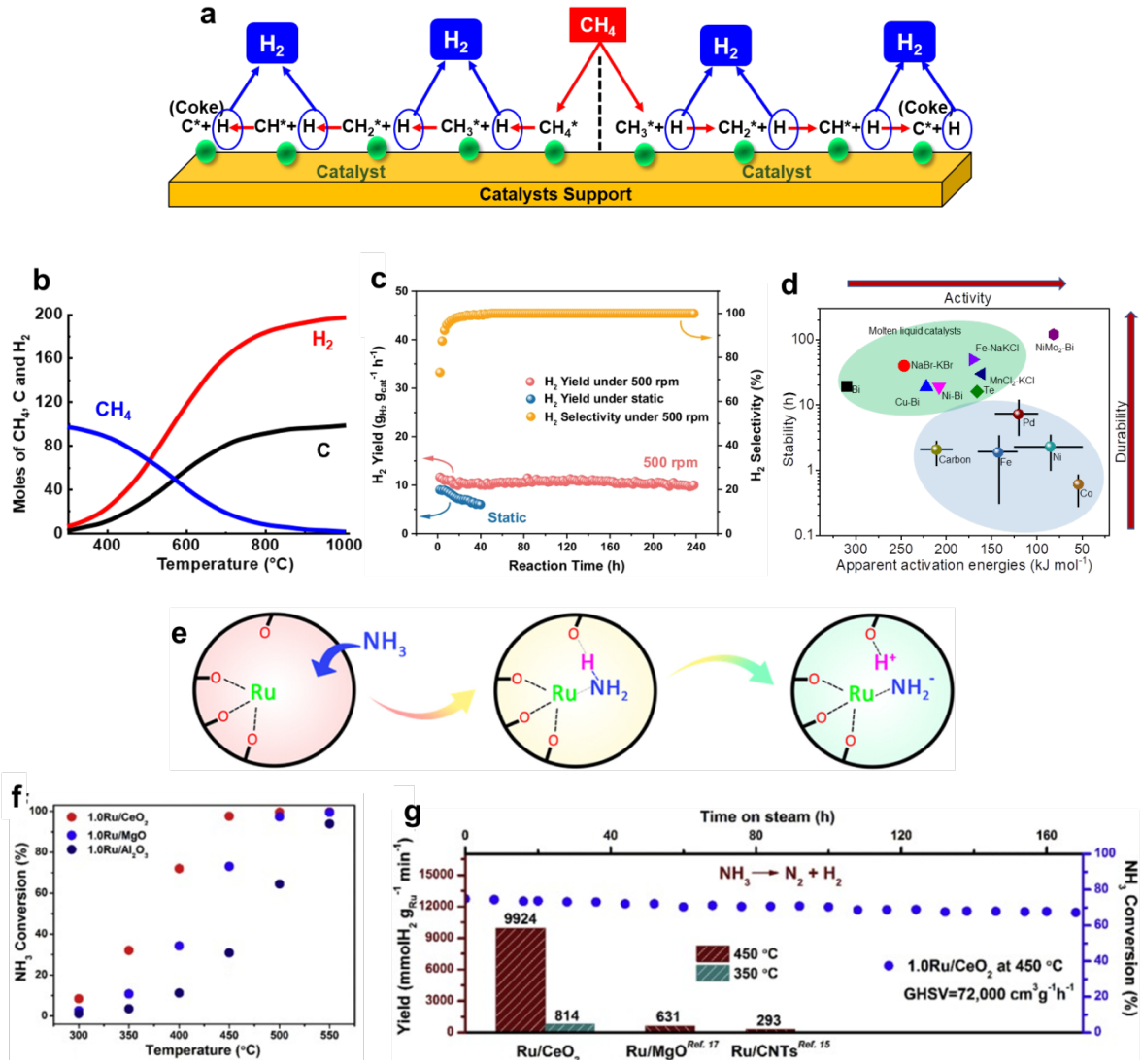

Fig. 5. CH_4 pyrolysis and NH_3 cracking mechanism and catalytic performance. a) Adsorptive and dissociative reaction pathways. **b)** Reaction equilibrium curves[54,55]. **c)** Long-term study of CH_4 decomposition over Re/Ni SAA at 450 °C and 500 rpm vibration frequency of ball milling in 50 mL min^{-1} CH_4[ref.114]. **d)** Overview of catalysts for H_2 production from CH_4 pyrolysis, including the stability and activity of different solid and molten liquid catalysts[115]. **e)** Proposed FLP-type mechanism for the N–H cleavage over the Ru sites in 13X zeolite[11]. **f,g)** NH_3 conversion against temperature with GHSV of 22,000 mL g^{-1} h^{-1} (f) and H_2 yield and stability at 450 °C with GHSV of 124,000 mL g^{-1} h^{-1} over Ru-based catalysts (g)[37].

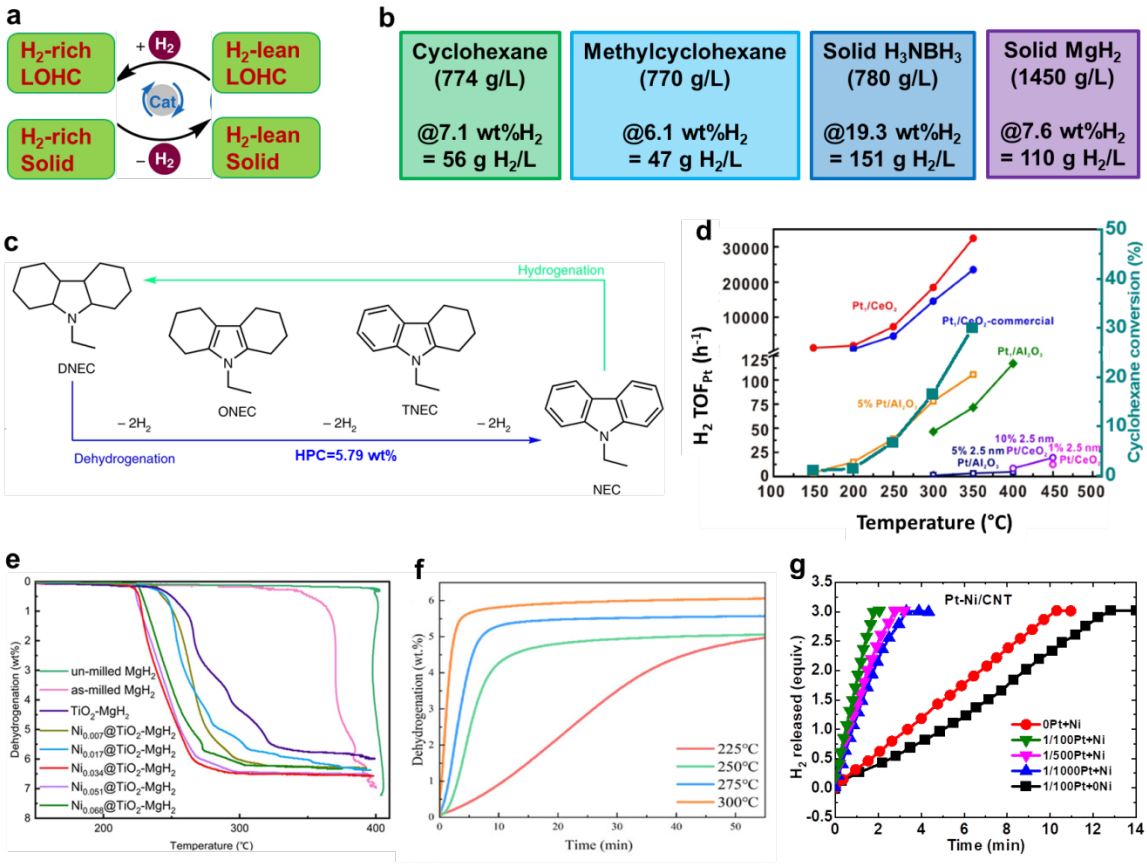

Fig. 6. Direct dehydrogenation of reversible liquid-to-liquid and solid-to-solid substances. a,b) Typical H_2 stores with relevant mass and volume-based capacities. **c)** Schematic pathway of 12H–NEC dehydrogenation[33]. **d)** TOF of H_2 generation from CH dehydrogenation with conversion against temperature; under 100 mg catalyst and 3 mL h^{-1} CH feed rate[32]. **e,f)** Temperature-programmed desorption curves of $Ni_x@TiO_2$–MgH_2 (x = 0.007, 0.017, 0.034, 0.051, 0.068) (e)[47] and dehydrogenation curves and e) hydrogenation curves of 15 wt.%-$Ru_{0.028}@Nb_2O_5$-MgH_2 at various temperatures (f)[133]. **g)** Dehydrogenation kinetics of AB over Pt-catalysts at 25 °C[139].

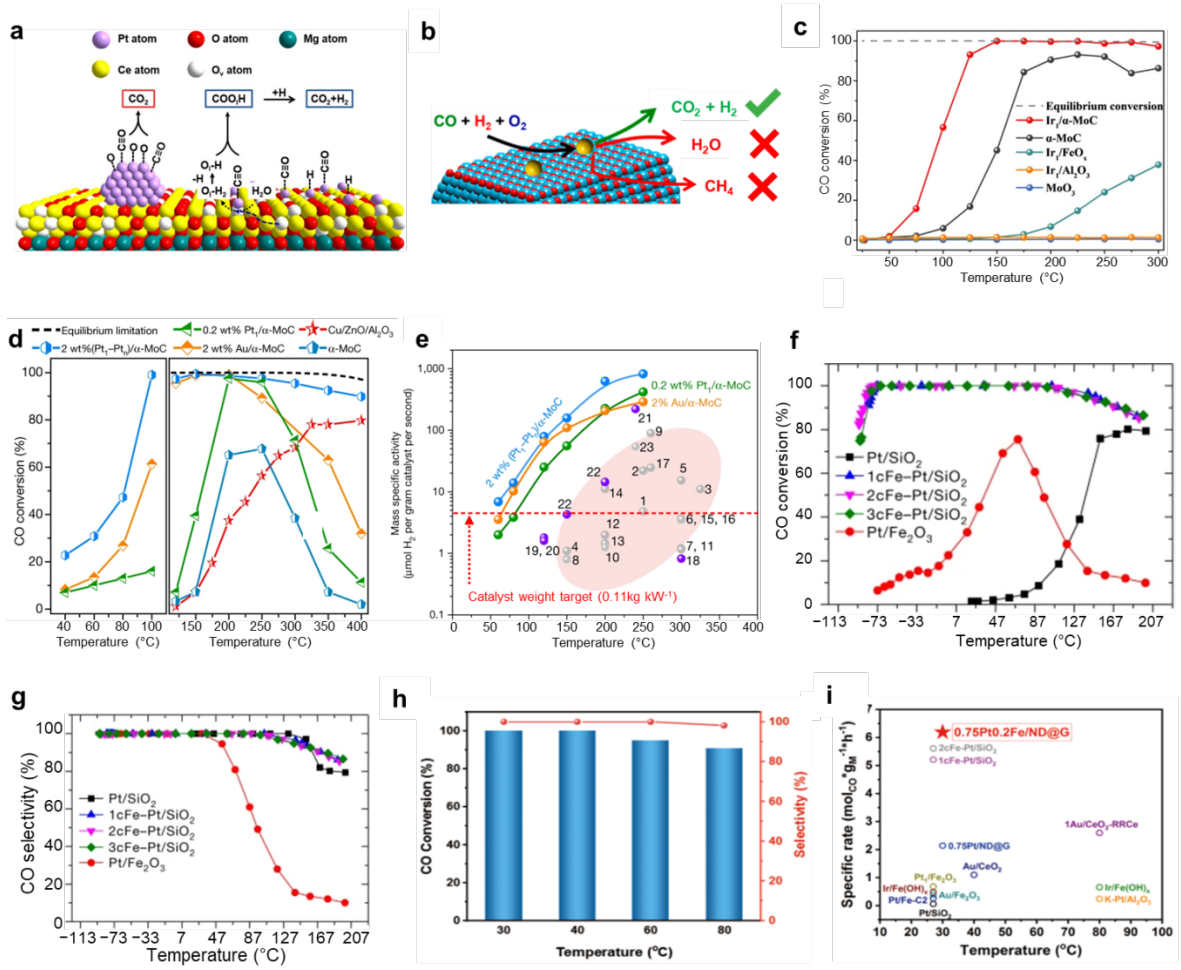

Fig. 7. WGS and CO PROX mechanism and performance of SACs. a) Schematic CO oxidation description by Pt_{NP} or Pt_1 anchored to $CeO_{2-\delta}/MgO$[152]. **b)** CO PROX pathway over CO oxidation[177]. **c)** CO conversion over Ir-SACs against temperature, under 2% CO, 10% H_2O with 18,000 mL g^{-1} h^{-1}[ref.166]. **d)** CO conversion over (Pt_1–Pt_n)/α-MoC against temperature (40 to 100 °C: 3% CO, 6% H_2O at 180,000 h^{-1}; 120 to 400 °C: 10.5% CO, 21% H_2O at 180,000 h^{-1}); dotted line is CO thermodynamic equilibrium conversion[35]. **e)** Summary of mass-specific activities of typical metal/oxide catalysts (grey points, shaded in light pink), metal/β–Mo_2C catalysts (purple points), Au/α–MoC catalysts (orange points), 0.2 wt% Pt_1/α–MoC (dark green points) and 2 wt% (Pt_1–Pt_n)/α-MoC (light-blue points) catalysts (please to the ref. 35 for the cited data literature)[35]. **f,g)** CO-PROX (f) and CO selectivity (g). Reaction conditions: 1% CO, 0.5% O_2 and 48% H_2 balanced in helium at 1 bar and SV = 36,000 mL g^{-1} h^{-1}[181]. **h)** CO conversion and selectivity of 0.75Pt0.2Fe/ND@G catalyst in PROX reaction. Reaction conditions: 1% CO, 0.5% O_2 and 48% H_2 balanced in He; the space velocity is 45000 mL g^{-1} h^{-1}[183]. **i)** Comparison of the specific rate with reported metal catalysts as a function of their reaction temperature in PROX reaction[183].

Acknowledgements

This work was supported by EPSRC (grants EP/W033321/1; EP/W03395X/1; EP/X023656/1) and Science Specialty Program of Sichuan University (Grant. No. 2020SCUNL210).

Glossary terms

Net zero

The balance between the amount of greenhouse gas released to and the amount removed from the atmosphere.

Steam reforming methane
A process in which methane is heated with steam over a catalyst to produce a mixture of carbon monoxide and hydrogen (called synthesis gas or syngas).

Water-gas shift
Describes the reaction of carbon monoxide and *water* vapor to form carbon dioxide and hydrogen, thus often applied in hydrocarbon reforming to eliminate CO and generate excess hydrogen.

Dry reforming
A process that avoids steam and produces synthesis gas from the reaction of two greenhouse gases, carbon dioxide and methane.

TOF
Defined as the turnover number (TON)/time of reaction, which is equivalent to moles of desired product formed per moles of catalyst per time

X-ray absorption spectroscopy (XAS)
An experimental technique that determines the local geometric and/or electronic structure of matter and the experiment is usually performed at synchrotron radiation facilities.

X-ray photoemission spectroscopy (XPS)
It is a surface-sensitive quantitative analysis method to determine the elemental composition as well as the chemical and electronic state of the atoms of solid materials.

References

1. Meinshausen, M., Lewis, J., McGlade, C. *et al.* Realization of Paris Agreement pledges may limit warming just below 2 °C. *Nature* **604**, 304–309 (2022).
2. International energy agency. Net zero by 2050: A roadmap for the global energy sector (2021). https://www.iea.org/reports/net-zero-by-2050.
3. UK hydrogen strategy (2021). https://www.gov.uk/government/publications/uk-hydrogen-strategy.
4. U.S. to sharply cut methane pollution that threatens the climate and public health (2021). https://www.epa.gov/newsreleases/us-sharply-cut-methane-pollution-threatens-climate-and-public-health.
5. Cushing, L. J., Li, S., Steiger, B. B., Casey, J. A. Historical red-lining is associated with fossil fuel power plant siting and present-day inequalities in air pollutant emissions. *Nat Energy* **8**, 52–61 (2022).
6. Yang, X., Nielsen, C. P., Song, S., McElroy, M. B. Breaking the hard-to-abate bottleneck in China's path to carbon neutrality with clean hydrogen. *Nat Energy* **7**, 955–965 (2022).
7. International energy agency. Global hydrogen review (2021). https://www.iea.org/reports/global-hydrogen-review-2021.
8. Castelvecchi, D. How the hydrogen revolution can help save the planet — and how it can't. *Nature* **611**, 440–443 (2022).
9. Woodall, C. M., Fan, Z., Lou, Y. *et al.* Technology options and policy design to facilitate decarbonization of chemical manufacturing. *Joule* **6**, 2474–2499 (2022).
10. Zeng, L., Cheng, K., Sun, F. *et al.* Stable anchoring of single rhodium atoms by indium in zeolite alkane dehydrogenation catalysts. *Science* **383**, 998–1004 (2024).
11. Leung, K. C., Hong, S., Li, G. *et al.* Confined Ru sites in a 13X zeolite for ultrahigh H_2 production from NH_3 decomposition. *J Am Chem Soc* **145**, 14548−14561 (2023).
12. X. *et al.* Shielding Pt/γ-Mo_2N by inert nano-overlays enables stable H_2 production. *Nature* **638**, 690–696 (2025).
13. Zhou, C., Zhang, Y., Li, B., Yang, B., Li, L. Resolving the active role of isolated transition metal species in Ni-based catalysts for dry reforming of methane. *ACS Catal* **14**, 4164–4174 (2024).
14. Wang, H., Hui, Y., Niu, Y. *et al.* Construction of $Pt^{\delta+}$–O(H)–Ti^{3+} species for efficient catalytic production of hydrogen. *ACS Catal* 13, 10500–10510 (2023).
15. Chen, Y., Kong, X., Yang, C. *et al.* A catalytic cycle that enables crude hydrogen separation, storage and transportation. *Nat Energy* **10**, 971–980 (2025).

16. Lee, W.H., Park, H., Lee, C.W. *et al.* Polymeric stabilization at the gas–liquid interface for durable solar hydrogen production from plastic waste. *Nat. Nanotechnol.* **20**, 1237–1246 (2025).
17. Wang, Y., Liu, B., Guo, Q. *et al.* Stabilized *OH species by K^+-doped Pt for H_2 generation with ultra-low levels of CO through aqueous-phase reforming of methanol at low temperature. *Appl Catal B: Environ Energy* **338**, 123011 (2023).
18. Li, Q., Sun, Z., Wei, Y. *et al.* Acceptorless ambient-temperature dehydrogenation and reversible hydrogenation of N-heterocycles over single-atom Co-N-C catalysts. *Appl Catal B: Environ Energy* **351**, 123959 (2024).
19. Meng, H., Yang, Y., Shen, T. *et al.* A strong bimetal-support interaction in ethanol steam reforming. *Nat Commun* **14**, 3189 (2023).
20. Ge, L., Zhu, Y., Qiu, M. *et al.* A highly active Pd clusters hosted by magnesium hydroxide nanosheets promoting hydrogen storage. *Appl Catal B: Environ Energy* **333**, 122793 (2023).
21. Meng, H., Yang, Y., Shen, T. Highly efficient hydrogen production from dehydrogenation reaction of nitrogen heterocycles *via* Pd^0–$Pd^{\delta+}$ synergistic catalysis. *ACS Catal* **13**, 9234–9244 (2023).
22. Li, X., Mitchell, S., Fang, Y. *et al.* Advances in heterogeneous single-cluster catalysis. *Nat Rev Chem* **7**, 754–767 (2023).
23. Cheng, K., Smulders, L. C. J., van der Wal, L. I. *et al.* Maximizing noble metal utilization in solid catalysts by control of nanoparticle location. *Science* **377**, 204–208 (2022).
24. Li, X., Pereira-Hernández, X. I., Chen, Y. *et al.* Functional CeO_x nanoglues for robust atomically dispersed catalysts. *Nature* **611**, 284–288 (2022).
25. Wang, A., Li, J., Zhang, T. Heterogeneous single-atom catalysis. *Nat Rev Chem* **2**, 65–81 (2018).
26. Sarma, B. B., Maurer, F., Doronkin, D. E., Grunwaldt, J. D. Design of single-atom catalysts and tracking their fate using operando and advanced X-ray spectroscopic tools. *Chem Rev* **123**, 379–444 (2023).
27. Li, J., Stephanopoulos, M. F., Xia, Y. Introduction: heterogeneous single-atom catalysis. *Chem Rev* **120**, 11699–11702 (2020).
28. Qiao, B., Wang, A., Yang, X. *et al.* Single-atom catalysis of CO oxidation using Pt_1/FeO_x. *Nat Chem* **3**, 634–641 (2011).
29. Lin, L., Zhou, W., Gao, R. *et al.* Low-temperature hydrogen production from water and methanol using Pt/α-MoC catalysts. *Nature* **544**, 80–83 (2017).
30. Meng, Y., Sun, Q., Zhang, T. *et al.* Cobalt-promoted noble-metal catalysts for efficient hydrogen generation from ammonia borane hydrolysis. *J Am Chem Soc* **145**, 5486–5495 (2023).
31. Zhang, S., Liu, Y., Zhang, M. *et al.* Sustainable production of hydrogen with high purity from methanol and water at low temperatures. *Nat Commun* **13**, 5527 (2022).
32. Chen, L., Verma, P., Hou, K. *et al.* Reversible dehydrogenation and rehydrogenation of cyclohexane and methylcyclohexane by single-site platinum catalyst. *Nat Commun* **13**, 1092 (2022).
33. Dong, C., Gao, Z., Li, Y. *et al.* Fully exposed palladium cluster catalysts enable hydrogen production from nitrogen heterocycles. *Nat Catal* **5**, 485–493 (2022).
34. Deng, Y., Guo, Y., Jia, Z. *et al.* Few-atom Pt ensembles enable efficient catalytic cyclohexane dehydrogenation for hydrogen production. *J Am Chem Soc* **144**, 3535–3542 (2022).
35. Zhang, X., Zhang, M., Deng, Y. *et al.* A stable low-temperature H_2-production catalyst by crowding Pt on α-MoC. *Nature* **589**, 396–401 (2021).
36. Yang, J., Fu, W., Chen, C. *et al.* Atomic design and fine-tuning of subnanometric Pt catalysts to tame hydrogen generation. *ACS Catal* **11**, 4146–4156 (2021).
37. Hu, X. C., Fu, X. P., Wang, W. W. *et al.* Ceria-supported ruthenium clusters transforming from isolated single atoms for hydrogen production via decomposition of ammonia. *Appl Catal B: Environ Energy* **268**, 118424 (2020).
38. Han, J.-T., Xue, Z.-H., Zhang, K. *et al.* Atomically dispersed Ni-based anti-coking catalysts for methanol dehydrogenation in a fixed-bed reactor. *ACS Catal* **10**, 12569–12574 (2020).
39. Cao, S., Yang, M., Elnabawy, A. O. *et al.* Single-atom gold oxo-clusters prepared in alkaline solutions catalyse the heterogeneous methanol self-coupling reactions. *Nat Chem* **11**, 1098–1105 (2019).
40. Chen, L. N., Hou, K. P., Liu, Y. S. *et al.* Efficient hydrogen production from methanol using a single-site Pt_1/CeO_2 catalyst. *J Am Chem Soc* **141**, 17995–17999 (2019).
41. Li, J., Guan, Q., Wu, H. *et al.* Highly active and stable metal single-atom catalysts achieved by strong electronic metal–support interactions. *J Am Chem Soc* **141**, 14515–14519 (2019).
42. Chen, Y., Lin, J., Li, L. *et al.* Identifying size effects of Pt as single atoms and nanoparticles supported on FeO_x for the water-gas shift reaction. *ACS Catal* **8**, 859–868 (2018).
43. Yan, H., Lin, Y., Wu, H. *et al.* Bottom-up precise synthesis of stable platinum dimers on graphene. *Nat Commun* **8**, 1070 (2017).
44. Lin, J., Wang, A., Qiao, B. *et al.* Remarkable performance of Ir_1/FeO_x single-atom catalyst in water gas shift reaction. *J Am Chem Soc* **135**, 15314–15317 (2013).
45. Wu, J., Gao, J., Lian, S. *et al.* Engineering the oxygen vacancies enables Ni single-atom catalyst for stable and efficient C-H activation. *Appl Catal B: Environ Energy* **314**, 121516 (2022).
46. Shen, D., Li, Z., Shan, J. *et al.* Synergistic Pt-CeO_2 interface boosting low temperature dry reforming of methane. *Appl Catal B: Environ Energy* **318**, 121809 (2022).
47. Zhang, J., Wang, W., Chen, X. *et al.* Single-atom Ni supported on TiO_2 for catalyzing hydrogen storage in MgH_2. *J Am Chem Soc* **146**, 10432–10442 (2024).
48. Akira Oda, Nodoka Ogawa, Yuta Yamamoto, Kyoichi Sawabe, and Atsushi Satsuma, Atom-to-nm Scale Engineering of PtCo Alloy Catalysts over Supported Co Nanoparticles for Advanced Toluene Hydrogenation Efficiency in Hydrogen

Storage Applications, ACS Catalysis **2025** 15 (4), 3191-3202
49. R. Gu, T. Wang, Y. Ma, T.-X. Wang, R.-Q. Yao, Y. Zhao, Z. Wen, G.-F. Han, X.-Y. Lang, Q. Jiang, Upcycling Polyethylene to High-Purity Hydrogen under Ambient Conditions via Mechanocatalysis, *Angew. Chem. Int. Ed.* 2025, 64, e202417644.
50. Ling-Yu Yan, Xin-Pu Fu, Wei-Wei Wang, Chun-Jiang Jia, Atmosphere-induced Ru-Ov-CeO2 interface for alleviating hydrogen inhibitory effect toward ammonia decomposition, Applied Catalysis B: Environment and Energy, 378, 2025, 125538
51. Mi Peng *et al.*, Thermal catalytic reforming for hydrogen production with zero CO_2 emission. *Science***387**, 769-775 (2025).
52. He, Z., Li, K., Chen, T. *et al.* High-purity hydrogen production from dehydrogenation of methylcyclohexane catalyzed by zeolite-encapsulated subnanometer platinum-iron clusters. *Nat Commun* **16**, 92 (2025).
53. IEA: Global Hydrogen Review 2024. https://www.iea.org/reports/global-hydrogen-review-2024.
54. Ahmad, K., Polychronopoulou, K., Jaoude, M. A. CH_4 valorisation reactions: a comparative thermodynamic analysis and their limitations. *Fuel* **320**, 123877(2022).
55. Bion, N., Epron, F., Duprez, D. Bioethanol reforming for H_2 production. A comparison with hydrocarbon reforming. *Catal* **22**, 1–55 (2010).
56. Hydrogen production and natural gas reforming. Energy efficiency and renewable energy. https://www.energy.gov/eere/fuelcells/hydrogen-production-natural-gas-reforming
57. Chen, L., Qi, Z., Peng, X. *et al.* Insights into the mechanism of methanol steam reforming tandem reaction over CeO_2 supported single-site catalysts. *J Am Chem Soc* **143**, 12074–12081 (2021).
58. Duarte, R. B., Krumeich, F., Bokhoven, J. A. V. Structure, activity, and stability of atomically dispersed Rh in methane steam reforming. *ACS Catal* **4**, 1279–1286 (2014).
59. Meng, H., Yang, Y., Shen, T. *et al.* Designing Cu^0–Cu^+ dual sites for improved C−H bond fracture towards methanol steam reforming. *Nat Commun* **14**, 7980 (2023).
60. Zhang, X., Yim, K., Kim, J., Wu, D., Ha, S. Elucidating the promoting role of Mo_2C in methane activation using Ni-xMo_2C/FAU to catalyze methane steam reforming. *Appl Catal B: Environ Energy* **310**, 121250 (2022).
61. Tusini, E., Casapu, M., Zimina, A. *et al.* Structural changes of Ni and Ni–Pt methane steam reforming catalysts during activation, reaction, and deactivation under dynamic reaction conditions. *ACS Catal* **14**, 7463–7477 (2024).
62. Yuan, D., Peng, Y., Ma, L. *et al.* Coke and sintering resistant nickel atomically doped with ceria nanosheets for highly efficient solar driven hydrogen production from bioethanol. *Green Chem* **24**, 2044–2050 (2022).
63. Yan, G., Tang, Y., Li, Y. *et al.* Reaction product-driven restructuring and assisted stabilization of a highly dispersed Rh-on-ceria catalyst. *Nat Catal* **5**, 119–127 (2022).
64. Lin, L., Yu, Q., Peng, M. *et al.* Atomically dispersed Ni/α-MoC catalyst for hydrogen production from methanol/water. *J Am Chem Soc* **143**, 309–317 (2021).
65. Mao, Q., Guo, Y., Liu, X. *et al.* Identifying the realistic catalyst for aqueous phase reforming of methanol over Pt supported by lanthanum nickel perovskite catalyst. *Appl Catal B: Environ Energy* **313**, 121435 (2022).
66. *Z Wei, S Shi, F Dong, H Jia, Z Chen, and B Yin, Regulating Heteroatom Doping-Induced Embedded Pt-M Bimetallic Sites Coupled with Ce^{3+}-OVs for Efficient Low-Temperature Methanol Steam Reforming, ACS Catalysis **2025** 15, 1002-1017*
67. Zhang, S., Zhou, H., Shao, Z. *et al.* Phase-interface-anchored cadmium single-atom catalysts for efficient methanol steam reforming. *Nat Commun* **16**, 7739 (2025).
68. Sun, Z., Shi, W., Smith, L.R. *et al.* Concerted catalysis of single atom and nanocluster enhances bio-ethanol activation and dehydrogenation. *Nat Commun* **16**, 3935 (2025).
69. Alipour, Z., Borugadda, V. B., Wang, H., Dalai, A. K. Syngas production through dry reforming: a review on catalysts and their materials, preparation methods and reactor type. *Chem Eng J* **452**, 139416 (2023).
70. Zhou, L., Martirez, J. M. P., Finzel, J. *et al.* Light-driven methane dry reforming with single atomic site antenna-reactor plasmonic photocatalysts. *Nat Energy* **5**, 61–70 (2020).
71. Song, Y., Ozdemir, E., Ramesh, S. *et al.* Dry reforming of methane by stable Ni–Mo nanocatalysts on single-crystalline MgO. *Science* **367**, 777–781 (2020).
72. Palmer, C., Upham, D. C., Smart, S. *et al.* Dry reforming of methane catalysed by molten metal alloys. *Nat Catal* **3**, 83–89 (2020).
73. Deng, J., Bu, K., Shen, Y. *et al.* Cooperatively enhanced coking resistance via boron nitride coating over Ni-based catalysts for dry reforming of methane. *Appl Catal B: Environ Energy* **302**, 120859 (2022).
74. D. He, Y. Zhang, T. Li, D. Chen, H. Wang, L. Zhang, J. Liu, X. Cao, J. Lu, Y. Luo, Designing Ultra-Stable and Surface-Exposed Ni Nanoparticles with Dually Confined Microenvironment for High-Temperature Methane Dry Reforming. *Adv. Funct. Mater.* 2025, 35, 2412895.
75. J. Yang, Z. Cao, Y. Wan, S. Guan, B. Jiang, Y. Yamauchi, H. Li, Vacancy-Anchored Sub-Nanometer Ru Catalyst with High Activity and Strong Durability at 800 °C Dry Reforming of Methane. *Adv. Energy Mater.* 2025, 15, 2404936.
76. Akri, M., Zhao, S., Li, X. *et al.* Atomically dispersed nickel as coke-resistant active sites for methane dry reforming. *Nat Commun* **10**, 5181 (2019).
77. Li, J., Du, C., Feng, Q. *et al.* Evolution and performances of Ni single atoms trapped by mesoporous ceria in dry reforming of methane. *Appl Catal B: Environ Energy* **354**, 124069 (2024).
78. Wang, H., Hu, Y., Adogwa, A. *et al.* The *in-situ* growth of atomically dispersed Ni species on CeO_2 during low-temperature CH_4/CO_2 reforming. *J Mater Chem A* **12**, 23530–23540 (2024).

79. Cheng, Q., Yao, X., Ou, L. *et al.* Highly efficient and stable methane dry reforming enabled by a single-site cationic Ni catalyst. *J Am Chem Soc* **145,** 25109–25119 (2023).
80. Tang, Y., Wei, Y., Wang, Z. *et al.* Synergy of single-atom Ni_1 and Ru_1 sites on CeO_2 for dry reforming of CH_4. *J Am Chem Soc* **141**, 7283–7293 (2019).
81. Kim, S., Lauterbach, J., Sasmaz, E. Yolk–shell Pt-NiCe@SiO_2 single-atom-alloy catalysts for low-temperature dry reforming of methane. *ACS Catal* **11**, 8247–8260 (2021).
82. Lv, H., Dong, X., Li, R. *et al.* Super-dry reforming of methane using a tandem electro-thermocatalytic system. *Nat. Chem.* **17**, 695–702 (2025).
83. Rao, Z., Wang, K., Cao, Y. *et al.* Light-reinforced key intermediate for anticoking to boost highly durable methane dry reforming over single atom Ni active sites on CeO_2. *J Am Chem Soc* **145,** 24625–24635 (2023).
84. Yang, H., Yu, R., Fang, Y. *et al.* Singly dispersed Ir_1Ti_3 bimetallic site for partial oxidation of methane at high temperature. *Appl Surf Sci* **599**, 153863 (2022).
85. Xu, Y., Yao, J., Lin, H. *et al.* Functional CeO_x stabilized metallic Ni catalyst supported on boron nitride for durable partial oxidation of methane to syngas at high temperature. *ACS Catal* **14,** 11845–11856 (2024).
86. Ding, S., Chen, H.-A., Mekasuwandumrong, O. *et al.* High-temperature flame spray pyrolysis induced stabilization of Pt single-atom catalysts. *Appl Catal B: Environ Energy* **281**, 119471 (2021).
87. Tang, Y., Fung, V., Zhang, X. *et al.* Single-atom high-temperature catalysis on a Rh_1O_5 cluster for production of syngas from methane. *J Am Chem Soc* **143**, 16566–16579 (2021).
88. Ding, Z., Chen, S., Yang, T. *et al.* Atomically dispersed MoNi alloy catalyst for partial oxidation of methane. *Nat Commun* **15**, 4636 (2024).
89. Liu, R., Zhang, X., Liu, T. *et al.* Dynamic oxygen migration and reaction over ceria-supported nickel oxides in chemical looping partial oxidation of methane. *Appl Catal B: Environ Energy* **328**, 122478 (2023).
90. Yao, X., Cheng, Q., Bai, X. *et al.* Enlarging the three-phase boundary to raise CO_2/CH_4 conversions on exsolved Ni–Fe alloy perovskite catalysts by minimal Rh doping. *ACS Catal* **14**, 5639–5653 (2024).
91. Zhang, X., Deng, J., Pupucevski, M. *et al.* High-performance binary Mo-Ni catalysts for efficient carbon removal during carbon dioxide reforming of methane. *ACS Catal* **11**, 12087–12095(2021).
92. *Yani Zhang, Ning Cao, Ke Wang, Mi Yan, Xingwang Zhang, and Pengfei Xie, Atomically Dispersed Rh–O–V Pairs Promote Methane Dry Reforming with Sustained Catalytic Activity, ACS Catalysis **2025** 15 (11), 8833-8845.*
93. Yu, J., Le, T., Jing, D. *et al.* Balancing elementary steps enables coke-free dry reforming of methane. *Nat Commun* **14**, 7514 (2023).
94. Sandoval-Diaz, L., Cruz, D., Vuijk, M. *et al.* Metastable nickel–oxygen species modulate rate oscillations during dry reforming of methane. *Nat Catal* **7**, 161–171 (2024).
95. Wang, H., Cui, G., Lu, H. *et al.* Facilitating the dry reforming of methane with interfacial synergistic catalysis in an Ir@CeO_{2-x} catalyst. *Nat Commun* **15**, 3765 (2024).
96. Lucas, J., Naveen, N. S. P., Janik, M. J. *et al.* Improved selectivity and stability in methane dry reforming by atomic layer deposition on Ni-CeO_2–ZrO_2/Al_2O_3 catalysts. *ACS Catal* **14**, 9115–9133 (2024).
97. Wei, D., Shi, X., Qu, R. *et al.* Toward a hydrogen economy: development of heterogeneous catalysts for chemical hydrogen storage and release reactions. *ACS Energy Lett* **7**, 3734–3752 (2022).
98. Tan, Z., Fan, G., Zheng, L., Li, F. Promoted surface-interface catalysis over Mn-Cr incorporated Cu-based catalysts for efficient hydrogen production from methanol decomposition. *ACS Catal* **14,** 11218–11230 (2024).
99. Cai, F., Guo, Y., Ibrahim, J. J., Zhang, J., Sun, Y. A highly active and stable Pd/MoC catalyst for hydrogen production from methanol decomposition. *Appl Catal B: Environ Energy* **299**, 120648 (2021).
100. Qi, Z., Chen, L., Zhang, S., Su, J., Somorjai, G. A. Mechanism of methanol decomposition over single-site Pt_1/CeO_2 catalyst: a DRIFTS study. *J Am Chem Soc* **143**, 60–64 (2021).
101. Y. Ge, Z. Gao, Y. Xu, M. Xu, X. Qin, M. Peng, S. Wang, R. Gao, W. Zhou, D. Ma, Inverting Methanol Dehydrogenation Selectivity by Crowding Atomic Ni Species over α-MoC Catalysts, *Angew. Chem. Int. Ed.* 2025, 64, e202423682.
102. Liu, H., Lei, Q., Miao, R. *et al.* Asymmetric coordination of single-atom Co sites achieves efficient dehydrogenation catalysis. *Adv Funct Mater* **32**, 2207408 (2022).
103. Li, X., Surkus, A.-E., Rabeah, J. *et al.* Cobalt single-atom catalysts with high stability for selective dehydrogenation of formic acid. *Angew Chem Int Ed* **59**, 15849–15854 (2020).
104. Shi, Y., Luo, B., Liu, R. *et al.* Atomically dispersed cobalt/copper dual-metal catalysts for synergistically boosting hydrogen generation from formic acid. *Angew Chem Int Ed* **62**, e202313099 (2023).
105. Guo, L., Zhuge, K., Yan, S. *et al.* Defect-driven nanostructuring of low-nuclearity Pt-Mo ensembles for continuous gas-phase formic acid dehydrogenation. *Nat Commun* **14**, 7518 (2023).
106. Anqi Zhang, Feifei Yang, Yixing Luo, Xiaomei Shen, Qilu Yao, Kun Wang, Jianhui Xia, Zhang-Hui Lu, Microenvironmental regulation of PdCo nanoclusters in mesoporous carbon enhances hydrogen production from formic acid, Applied Catalysis B: Environment and Energy, 373, 2025, 125360.
107. Z. Yang, G. Hou, N. Gao, Y. Li, X. Li, Z. Chen, H. Jin, M. Zhao, D. Wang, K. Chen, M. Antonietti, T. Liu, Z. Tian, Y. Zhang, Histidine-Based "Transfer Stations" at Carbon-Immobilized Metal Particles Enable Rapid Hydrogen Transfer for Efficient Formic Acid Dehydrogenation, *Angew. Chem. Int. Ed.* 2025, 64, e202501836.
108. D. Liu, H. Yao, H. Wang, X. Zhang, Z. Yang, C. Kong, B. Liu, Lewis Acidic VO_x Engineered PdAu Nanocatalysts for Efficient Formic Acid Dehydrogenation. *Adv. Energy Mater.* 2024, 15, 2402650.
109. Ouyang M, Papanikolaou KG, Boubnov A, Hoffman AS, Giannakakis G, Bare SR, et al. Directing reaction pathways via

in situ control of active site geometries in PdAu single-atom alloy catalysts. Nat Commun 2021;12:1549.
110. Exsoluted Ni from Hexaaluminates for CO_x Free Hydrogen and Carbon Nanotubes via the Catalytic Decomposition of Methane, *ACS Catal.* 2025, 15, 9220–9235.
111. Upham, D. C., Agarwal, V., Khechfe, A. *et al.* Catalytic molten metals for the direct conversion of methane to hydrogen and separable carbon. *Science* **358**, 917–921 (2017).
112. Xi, W., Wang, K., Shen, Y. *et al.* Dynamic co-catalysis of Au single atoms and nanoporous Au for methane pyrolysis. *Nat Commun* **11**, 1919 (2020).
113. Tu, R., Sun, J., Xu, Y. *et al.* Pt/Ni single-atom alloy boosts mechano-pyrolysis of alkane into hydrogen. *Appl Catal B: Environ Energy* **353**, 124085 (2024).
114. Sun, J., Tu, R., Xu, Y. *et al.* Machine learning aided design of single-atom alloy catalysts for methane cracking. *Nat Commun* **15**, 6036 (2024).
115. Chen, L., Song, Z., Zhang, S. *et al.* Ternary NiMo-Bi liquid alloy catalyst for efficient hydrogen production from methane pyrolysis. *Science* **381**, 857-861 (2023).
116. Sorcar, S. Rosen, B. A. Methane pyrolysis using a multiphase molten metal reactor. *ACS Catal* **13**, 10161–10166 (2023)
117. Han, S.J., Seo, J.-C., Park, G. *et al.* Novel descriptor-driven design of molten alloys for methane pyrolysis. *ACS Catal* **14**, 14787–14795 (2024).
118. Kim, J., Oh, C., Oh, H. *et al.* Catalytic methane pyrolysis for simultaneous production of hydrogen and graphitic carbon using a ceramic sparger in a molten NiSn alloy. *Carbon* **207**, 1–12 (2023).
119. MacFarlane, D. R., Cherepanov, P. V., Choi, J. *et al.* A roadmap to the ammonia economy. *Joule* **4**, 1186–11205 (2020).
120. Tabassum, H., Mukherjee, S., Chen, J. *et al.* Hydrogen generation via ammonia decomposition on highly efficient and stable Ru-free catalysts: approaching complete conversion at 450 °C. *Energy Environ Sci* **15**, 4190–4200 (2022).
121. Fang, H., Wu, S., Ayvali, T. *et al.* Dispersed surface Ru ensembles on MgO(111) for catalytic ammonia decomposition. *Nat Commun* **14**, 647 (2023).
122. Li, Y., Guan, Q., Huang, G. *et al.* Low temperature thermal and solar heating carbon-free hydrogen production from ammonia using nickel single atom catalysts. *Adv Energy Mater* **12**, 2202459 (2022).
123. Xiuzi He, Fang Dong, Chao Feng, Haitao Zhang, Yong Ding, Zhicheng Tang, The formation of Ru-O-Cs structure over Ru-based catalysts for efficient ammonia decomposition to hydrogen production, Nano Energy, 142, 2025, 111149
124. K. Xu, Y.-Y. Zhang, W.-W. Wang, M. Peng, J.-C. Liu, C. Ma, Y.-W. Zhang, C.-J. Jia, D. Ma, C.-H. Yan, Single-Atom Barium Promoter Enormously Enhanced Non-Noble Metal Catalyst for Ammonia Decomposition, *Angew. Chem. Int. Ed.* 2025, 64, e202416195.
125. Oda, A., Ichihashi, K., Yamamoto, Y. *et al.* Pt single atom alloyed sub-1 nm thick Fe overlayer on supported Cu nanoparticles for methylcyclohexane dehydrogenation. *J Mater Chem A* **12**, 22655–22667 (2024).
126. Li, L., Zhang, Q., Deng, C. *et al.* Pyridine N-induced intra-pore and interfacial dual-confined Pd^0-$Pd^{\delta+}$ synergistic catalysis for ultra-stable dehydrogenation of dodecahydro-N-propylcarbazole. *Appl Catal B: Environ Energy* **351**, 123987 (2024).
127. Lv, C., Lou, P., Chang, J., *et al.* Nickel single atoms/cerium oxide hybrid for hydrogen production via solar-heating catalytic dehydrogenation of methyl cyclohexane. *J. Power Sour.* **559**, 232674 (2023).
128. Y. Pang, X. Wan, Y. Li, M. Song, X. Liu, J. Shang, L. Zheng, J. Shui, Evolution of Nitrogen-Coordinated Metal Single Atoms Toward Single-Atom Alloys on MgH_2 as Efficient and Stable Hydrogen Spillover Catalysts. *Adv. Mater.* 2024, 36, 2412942.
129. Y. Li, L. Ren, Y. Yao, Y. Zhao, H. Xu, Z. Li, Z. Li, X. dai, Y. Tian, S. Cao, X. Lin, C. Ye, A. Züttel, J. Zou, A Single-Atom Interface Engineering Strategy to Promote Hydrogen Sorption Performances of Magnesium Hydride. *Adv. Funct. Mater.* 2025, 35, 2417915.
130. Yibo Qin, Longfei Chen, Meiying Dai, Yanfeng Zhu, Jiong Li, Wei Han, Wei Wei, Xinqing Chen, Hydroxyl-mediated palladium single-atom catalyst for highly efficient hydrogen storage, Applied Catalysis B: Environment and Energy, 379, 2025, 125742.
131. *Hongtao Wang, Kailang Li, Miguel Lopez-Haro, Carlo Marini, Zhe He, Minghao Gao, Liang Zhang, and Lichen Liu, Subnanometer Pt Catalysts Encapsulated in MEL Zeolite Mesocrystals for H_2 Production from Methylcyclohexane Dehydrogenation, Journal of the American Chemical Society* ***2025*** *147 (25), 21789-21802* .
132. H. Wu, H. Wang, Y. Lv, Y. Wu, Y. Wang, Q. Luo, Y. Hui, L. Liu, M. Zhang, K. Hou, L. Li, J. Zeng, W. Dai, L. Wang, F.-S. Xiao, Ultra-small Metallic Nickel Nanoparticles on Dealuminated Zeolite for Active and Durable Catalytic Dehydrogenation, *Angew. Chem. Int. Ed.* 2025, 64, e202420306.
133. B. Jia, J. Zhang, X Chen, J. Zhang, B. Han, W. Wang, X. Yan, J. Shui, J. Huang, Electronic Structure Modulation of Nb_2O_5 by Ru Single Atoms Enabling Efficient Hydrogen Storage of Magnesium Hydrides, *Angew. Chem. Int. Ed.* 2025, 64, e202511139.
134. Srinivas G, Ford J, Zhou W, Yildirim T. Zn-MOF assisted dehydrogenation of ammonia borane: Enhanced kinetics and clean hydrogen generation. Int J Hydrogen Energy 2012;37:3633–8.
135. Srinivas G, Travis W, Ford J, Wu H, Guo ZX, Yildirim T. Nanoconfined ammonia borane in a flexible metal–organic framework Fe–MIL-53: clean hydrogen release with fast kinetics. J Mater Chem A 2013;1:4167–72.
136. Sun, Q., Wang, X., Wang, H. *et al.* Crystal facet effects of platinum single-atom catalysts in hydrolytic dehydrogenation of ammonia borane. *J Mater Chem A* **10**, 10837–10843 (2022).
137. Guan, S., Yuan, Z., Zhao, S. *et al.* Efficient hydrogen generation from ammonia borane hydrolysis on a tandem ruthenium–platinum–titanium catalyst. *Angew Chem Int Ed* **63**, e202408193 (2024).

138. Chen, S., Gong, B., Gu, J. *et al.* Dehydrogenation of ammonia borane by platinum-nickel dimers: regulation of heteroatom interspace boosts bifunctional synergetic catalysis. *Angew Chem Int Ed* **61**, e202211919 (2022).
139. Li, Z., He, T., Matsumura, D., Miao, S. *et al.* Atomically dispersed Pt on the surface of Ni particles: Synthesis and catalytic function in hydrogen generation from aqueous ammonia-borane. *ACS Catal* **7**, 6762–6769 (2017).
140. Mekkering, M.J., Laan, P.C.M., Troglia, A. *et al.* Bottom-up synthesis of platinum dual-atom catalysts on cerium oxide. *ACS Catal* **14**, 9850–9859 (2024).
141. Chen, W., Shi, Y., Liu, C. *et al.* Restructuring the interfacial active sites to generalize the volcano curves for platinum-cobalt synergistic catalysis. *Nat Commun* **15**, 8995 (2024).
142. Chen, Y., Lang, Z., Feng, K. *et al.* Practical H_2 supply from ammonia borane enabled by amorphous iron domain. *Nat Commun* **15**, 9113 (2024).
143. Poon, P.-C., Wang, Y., Li, W. *et al.* Synergistic effect of Co catalysts with atomically dispersed CoN_x active sites on ammonia borane hydrolysis for hydrogen generation. *J Mater Chem A* **10**, 5580–5592 (2022).
144. Zhu, Y., Zeng, L., Wu, D. *et al.* MgH_2@$Mg(BH_4)_2$ core−shell-like nanostructures: synthesis, hydrolysis performance, and promotion mechanism. *Nano Lett* **24**, 3221−3230 (2024).
145. Zhou, S., Cheng, L., Huang, Y. *et al.* Constructing Ru particles decorated Co_3B-CoP heterostructures as a highly active and reusable catalyst for H_2 generation by catalyzing $NaBH_4$ hydrolysis. *Appl Catal B: Environ Energy* **328**, 122519 (2023).
146. Wang, J., Huang, Z., Lu, L. *et al.* Colloidal Co single-atom catalyst: a facile synthesis strategy and high catalytic activity for hydrogen generation. *Green Chem* **22**, 1269–1274 (2020).
147. Wang, Y., Li, J. L., Shi, W. X. *et al.* Unveiling single atom nucleation for isolating ultrafine fcc Ru nanoclusters with outstanding dehydrogenation activity. *Adv Energy Mater* **10**, 2002138 (2020).
148. Zhaolu Feng, Fangqin Guo, Yawen Zhang, Takayuki Ichikawa, Jie Zheng, Oxygen vacancies rich CeO2 supported Ru catalyst for efficient hydrogenation of N-ethylcarbazole at mild temperature, Applied Catalysis B: Environment and Energy, 366, 2025, 125059
149. Sutton, A. D., Burrell, A. K., Dixon, D. A. *et al.* Regeneration of ammonia borane spent fuel by direct reaction with hydrazine and liquid ammonia. *Science* **331**, 1426–1429 (2011).
150. Wang, Y., Xue, Y., Züttel, A. Nanoscale engineering of solid-state materials for boosting hydrogen storage. *Chem Soc Rev* **53**, 972–1003 (2024).
151. Fu, X. P., Wu, C. P., Wang, W. W. *et al.* Boosting reactivity of water-gas shift reaction by synergistic function over CeO_{2-x}/CoO_{1-x}/Co dual interfacial structures. *Nat Commun* **14**, 6851 (2023).
152. Wang, Y., Ma, J., Wang, X. *et al.* Complete CO oxidation by O_2 and H_2O over Pt-$CeO_{2-\delta}$/MgO following Langmuir-Hinshelwood and Mars-van Krevelen mechanisms, respectively. *ACS Catal* **11**, 11820–11830 (2021).
153. Sun, L., Cao, L., Su, Y. *et al.* Ru_1/FeO_x single-atom catalyst with dual active sites for water gas shift reaction without methanation. *Appl Catal B: Environ Energy* **318**, 121841 (2022).
154. Cui, Z., Song, S., Liu, H. *et al.* Synergistic effect of Cu^+ single atoms and Cu nanoparticles supported on alumina boosting water-gas shift reaction. *Appl Catal B: Environ Energy* **313**, 121468 (2022).
155. Shi, J., Li, H., Genest, A. *et al.* High-performance water gas shift induced by asymmetric oxygen vacancies: gold clusters supported by ceria-praseodymia mixed oxides. *Appl Catal B: Environ Energy* **301**, 120789 (2022).
156. Kuai, L., Liu, L., Tao, Q. *et al.* High-areal density single-atoms/metal oxide nanosheets: a micro-gas blasting synthesis and superior catalytic properties. *Angew Chem Int Ed* **61**, e202212338 (2022).
157. Liang, J.-X., Lin, J., Liu, J. *et al.* Dual metal active sites in an Ir_1/FeO_x single-atom catalyst: a redox mechanism for the water-gas shift reaction. *Angew Chem Int Ed* **59**, 12868–12875 (2020).
158. Tang, Y., Liu, Z., Ye, R. *et al.* Selectively located Pt clusters on Au/CeO_2 for highly robust water-gas shift reaction via atomic layer deposition. *Appl Catal B: Environ. Energy* **356**, 124218 (2024).
159. Gao, M., Yang, Z., Zhang, H. *et al.* Ordered mesopore confined Pt nanoclusters enable unusual self-enhancing catalysis. *ACS Cent Sci* **8**, 1633–1645 (2022).
160. Z. Shui, F. Zhang, H. Yang, M. Zhao, Z. Zhao, G. Li, Z. Wei, G. Jiang, Z. Zhang, Z. Hao, Tailoring the Electronic Metal-Support Interaction of Single-Atom Platinum Catalysts for Boosting Water-Gas Shift Reaction. *Adv. Funct. Mater.* 2025, 35, 2415774.
161. Li, X., Wang, X., Beck, A. *et al.* Quantifying electronic and geometric effects on the activity of platinum catalysts for water-gas shift. *Nat Commun* **16**, 6641 (2025).
162. Yang, M., Liu, J., Lee, S. *et al.* A common single-site Pt(II)-$O(OH)_x$- species stabilized by sodium on “active” and “inert” supports catalyzes the water-gas shift reaction. *J Am Chem Soc* **137**, 3470–3473 (2015).
163. Zugic, B., Zhang, S., Bell, D. C., Tao, F., Flytzani-Stephanopoulos, M. Probing the low-temperature water-gas shift activity of alkali-promoted platinum catalysts stabilized on carbon supports. *J Am Chem Soc* **136**, 3238–3245 (2014).
164. Yang, M., Allard, L. F., Flytzani-Stephanopoulos, M. Atomically dispersed Au-$(OH)_x$ species bound on titania catalyze the low-temperature water-gas shift reaction. *J Am Chem Soc* **135**, 3768–3771 (2013).
165. Jin, C., Wang, B., Zhou, Y. *et al.* Gold atomic layers and isolated atoms on MoC for the low-temperature water gas shift reaction. *ACS Catal* **12**, 15648–15657 (2022).
166. Sun, L., Xu, J., Liu, X. *et al.* High-efficiency water gas shift reaction catalysis on α-MoC promoted by single-atom Ir species. *ACS Catal* **11**, 5942–5950 (2021).
167. Tang, N., Liu, D., Chen, S. *et al.* Pt atom-substituted MoC single-atom catalyst for enhancing H_2 production. *ACS Catal* **14**, 14297–14307 (2024).

168. Li, R., Shang, J., Wang, F. *et al.* Quantification and optimization of platinum–molybdenum carbide interfacial sites to enhance low-temperature water-gas shift reaction. *Nat Commun* **16**, 1098 (2025).
169. Li, XC., Wang, JH., Huang, TT. *et al.* Tunning valence state of cobalt centers in Cu/Co-CoO_{1-x} for significantly boosting water-gas shift reaction. *Nat Commun* **16**, 736 (2025).
170. T. G. Novak, A. E. Herzog, M. R. Buck, *et al.* Atomically dispersed nickel in CeO_2 aerogel catalysts completely suppresses methanation in the water-gas shift reaction. *Sci. Adv.***10**, eadr9120 (2024).
171. Zhou Y, Xie Z, Jiang J, Wang J, Song X, He Q, et al. Lattice-confined Ru clusters with high CO tolerance and activity for the hydrogen oxidation reaction. Nat Catal 2020;3:454–62.
172. Cai J, Liu Z, Cao K, Lang Y, Chu S, Shan B, et al. Highly dispersed Pt studded on CoO_x nanoclusters for CO preferential oxidation in H_2. J Mater Chem A 2020;8:10180–7.
173. Cao S, Zhao Y, Lee S, Yang S, Liu J, Giannakakis G, et al. High-loading single Pt atom sites [Pt-$O(OH)_x$] catalyze the CO PROX reaction with high activity and selectivity at mild conditions. Sci Adv 2020;6:eaba3809.
174. Liu J, Hensley AJR, Giannakakis G, Therrien AJ, Sukkar A, Schilling AC, et al. Developing single-site Pt catalysts for the preferential oxidation of CO: A surface science and first principles-guided approach. Appl Catal B Environ 2021;284:119716.
175. Wang Q, Gong J, Zhang H, Fan QY, Xue L, Wu J, et al. Co-promotion of two-type active sites: PtCux single-atom alloy and copper-ceria interface for preferential oxidation of CO. Appl Catal B Environ 2022;306:121117.
176. Xiang G, Zhao S, Wei C, Liu C, Fei H, Liu Z, et al. Atomically dispersed Au catalysts for preferential oxidation of CO in H_2-rich stream. Appl Catal B Environ 2021;296:120385.
177. Qiao B, Liu J, Wang YG, Lin Q, Liu X, Wang A, et al. Highly Efficient Catalysis of Preferential Oxidation of CO in H_2-Rich Stream by Gold Single-Atom Catalysts. ACS Catal 2015;5:6249–54.
178. J. Yu, B. Song, Y. Yang, T. Liu, Z. Li, Y. Han, X. Liu, H. Meng, L. Wang, L. Zheng, X. Zhang, W. Dai, M. Wei, Highly Active Pt-Fe Catalysts Towards CO Preferential Oxidation with an Ultra-Wide Temperature Window *Angew. Chem. Int. Ed.* 2025, 64, e202510593.
179. Chen Y, Wan Q, Cao L, Gao Z, Lin J, Li L, et al. Facet-dependent electronic state of Pt single atoms anchoring on CeO_2 nanocrystal for CO (preferential) oxidation. J Catal 2022;415:174–85.
180. Ma K, Liao W, Shi W, Xu F, Zhou Y, Tang C, et al. Ceria-supported Pd catalysts with different size regimes ranging from single atoms to nanoparticles for the oxidation of CO. J Catal 2022;407:104–14.
181. Cao L, Liu W, Luo Q, Yin R, Wang B, Weissenrieder J, et al. Atomically dispersed iron hydroxide anchored on Pt for preferential oxidation of CO in H_2. Nature 2019;565:631–5.
182. Sadykov II, Sushkevich VL, Krumeich F, Nuguid RJG, van Bokhoven JA, Nachtegaal M, et al. Platinum-Iron(II) Oxide Sites Directly Responsible for Preferential Carbon Monoxide Oxidation at Ambient Temperature: An Operando X-ray Absorption Spectroscopy Study**. Angew Chem Int Ed 2023;62:e202214032.
183. Jia Z, Qin X, Chen Y, Cai X, Gao Z, Peng M, et al. Fully-exposed Pt-Fe cluster for efficient preferential oxidation of CO towards hydrogen purification. Nat Commun 2022;13:6798.
184. Liang, X., Jin, X., Yu, S. *et al.* CO-resistant hydrogenation over noble metal/α-MoC catalyst. *Nat Commun* **16**, 4159 (2025).
185. Liu R, El Berch JN, House S, Meil SW, Mpourmpakis G, Porosoff MD. Reactive Separations of CO/CO_2 mixtures over Ru–Co Single Atom Alloys. ACS Catal 2023;13:2449–61.
186. Zhang, P., Wang, Q., Zhang, Y. *et al.* Strain-induced crumpling of graphene oxide lamellas to achieve fast and selective transport of H_2 and CO_2. *Nat. Nanotechnol.* **20**, 1254–1261 (2025)
187. Gadipelli S, Guo ZX. Graphene-based materials: Synthesis and gas sorption, storage and separation. Prog Mater Sci 2015;69:1–60.
188. Gadipelli S, Travis W, Zhou W, Guo Z. A thermally derived and optimized structure from ZIF-8 with giant enhancement in CO_2 uptake. Energy Environ Sci 2014;7:2232–8.
189. X. Tian, H. Huan, K. Zhang, R. Zhang, L. Liu, X. Liu, X. Zhang, Y. Yu, T. Gu, S. Wang, Z. Jiang, Building Unit Engineering Toward COF Membranes with Controlled Stacking for H_2 Purification. *Adv. Mater.* 2025, 37, 2504622.
190. Gadipelli S, Lu Y, Skipper NT, Yildirim T, Guo Z. Design of hyperporous graphene networks and their application in solid-amine based carbon capture systems. J Mater Chem A 2017;5:17833–40.
191. Gadipelli S, Patel HA, Guo Z. An Ultrahigh Pore Volume Drives Up the Amine Stability and Cyclic CO_2 Capacity of a Solid-Amine@Carbon Sorbent. Adv Mater 2015;27:4903–9.
192. Gadipelli S, Krungleviciute V, Guo Z-X, Yildirim T. Exceptional CO_2 capture in a hierarchically porous carbon with simultaneous high surface area and pore volume. Energy Environ Sci 2014;7:335–42.
193. McDonald TM, Mason JA, Kong X, Bloch ED, Gygi D, Dani A, et al. Cooperative insertion of CO_2 in diamine-appended metal-organic frameworks. Nature 2015;519:303–8.
194. Zhu Q, Zhou H, Wang L, Wang L, Wang C, Wang H, et al. Enhanced CO_2 utilization in dry reforming of methane achieved through nickel-mediated hydrogen spillover in zeolite crystals. Nat Catal 2022;5:1030–7.
195. Potential and possible applications of a climate friendly hydrogen production, **https://hydrogeneurope.eu/**
196. Öberg, S., Odenberger, M., Johnsson, F. The cost dynamics of hydrogen supply in future energy systems – a techno-economic study. *Appl Energy* **328,** 120233 (2022).
197. Kakran, S., Sidhu, A., Kumar, A., Youssef, A. B., Lohan, S. Hydrogen energy in BRICS-US: A whirl succeeding fuel treasure. *Appl Energy* **334,** 120670 (2023).
198. Kannah, R. Y., Kavitha, S., Karthikeyan, O. P. *et al.* Techno-economic assessment of various hydrogen production

methods – a review. *Bioresour Technol* **319,** 124175 (2021).
199. Guan, D., Wang, B., Zhang, J. *et al.* Hydrogen society: from present to future. *Energy Environ Sci* **16**, 4926–4943 (2023).
200. Niloufar Atashi, Adrià Palomares, Nicola Verziaggi, Luis Alves, Adelio Mendes, Simone Meloni, Gonzalo Prieto, Carbon-induced metal growth and size-dependent activity in methane splitting on nickel nanoparticle catalysts for COx-free hydrogen production, Applied Catalysis B: Environment and Energy, 381, 2026, 125817.
201. He, T., Pachfule, P., Wu, H. *et al.* Hydrogen carriers. *Nat Rev Mater* **1**, 16059 (2016).
202. Kar, S., Kim, D., Bin Mohamad Annuar, A. *et al.* Direct air capture of CO_2 for solar fuel production in flow. *Nat Energy* **10**, 448–459 (2025).
203. Ren R, Dou B, Zhang H, Wu K, Wang Y, Chen H, et al. Syngas production from CO_2 reforming of glycerol by mesoporous Ni/CeO_2 catalysts. Fuel 2023;341:127717.
204. *Charlotte Vogt, Jelle Kranenborg, Matteo Monai, and Bert M. Weckhuysen, Structure Sensitivity in Steam and Dry Methane Reforming over Nickel: Activity and Carbon Formation, ACS Catalysis* **2020** *10* (2), 1428-1438.
205. Recent advances in the catalysis of steam reforming of methane (SRM). International Journal of Hydrogen Energy, 51, Part C, 2024, 688-700.
206. IEA. Is carbon capture too expensive? – Analysis. https://www.iea.org/commentaries/is-carbon-capture-too-expensive
207. Comprehensive Review on Methane Pyrolysis for Sustainable Hydrogen Production, *Energy Fuels* 2024, 38, 15, 13514–13538.
208. Ge, L., Qiu, M., Zhu, Y. *et al.* Synergistic catalysis of Ru single-atoms and zeolite boosts high-efficiency hydrogen storage. *Appl Catal B: Environ Energy* **319**, 121958 (2022).
209. Xue, W., Liu, H., Zhao, B. *et al.* Single Rh_1Co catalyst enabling reversible hydrogenation and dehydrogenation of N-ethylcarbazole for hydrogen storage. *Appl Catal B: Environ Energy* **327**, 122453 (2023).
210. Yamazaki, K., Matsumoto, M., Ishikawa, M., Sato, A. NH_3 decomposition over Ru/CeO_2-PrO_x catalyst under high space velocity conditions for an on-site H_2 fueling station. *Appl Catal B Environ* **325,** 122352 (2023).
211. Tullo AH. Organics Challenge Ammonia as Hydrogen Carriers. ACS Cent Sci 2022;8:1471–3.
212. Tang, Y., Zhang, S., Rawal, T. B. *et al.* Atomic-scale structure and catalysis on positively charged bimetallic sites for generation of H_2. *Nano Lett* **20**, 6255–6262 (2020).
213. Jiang, T., Li, Y., Tang, Y. *et al.* Breaking continuously packed bimetallic sites to singly dispersed on nonmetallic support for efficient hydrogen production. *ACS Appl Mater Interf* **16**, 21757–21770 (2024).
214. Xuan Liang, Zirui Gao, Xingjie Peng, Maolin Wang, Yao Xu, Jie Zhang, Shuheng Tian, Chengyu Li, Xuetao Qin, Rongli Mi, Zhaohua Wang, Wu Zhou, Meng Wang, and Ding Ma, Efficient Hydrogen Production from Ethylene Glycol Steam Reforming Catalyzed by Na-Promoted Pt/γ-Mo_2N, *Journal of the American Chemical Society* **2025** *147* (37), 33395-33402.
215. Deciphering the role of Cu^0 and $Cu^{\sigma+}$ in engendering the hydrogen production from glycerol reforming over Cu/CeO_2: The effect of different Cu precursors, Applied Catalysis B: Environment and Energy, 365, 2025, 124865.
216. Zeng X, Fang M, Lv T, Tian J, Xia Z, Cen J, et al. Hydrogen-rich gas production by catalytic steam gasification of rice husk using CeO_2-modified Ni-CaO sorption bifunctional catalysts. Chem Eng J 2022;441:136023.
217. Jie X, Li W, Slocombe D, Gao Y, Banerjee I, Gonzalez-Cortes S, et al. Microwave-initiated catalytic deconstruction of plastic waste into hydrogen and high-value carbons. Nat Catal 2020;3:902–12.
218. Zhang K, Kim W-J, Park A-HA. Alkaline thermal treatment of seaweed for high-purity hydrogen production with carbon capture and storage potential. Nat Commun 2020;11:3783.
219. Shapiro-Bengtsen S, Hamelin L, Bregnbæk L, Zou L, Münster M. Should residual biomass be used for fuels, power and heat, or materials? Assessing costs and environmental impacts for China in 2035. Energy Environ Sci 2022;15:1950–66.
220. Li W, Qian K, Yang Z, Ding X, Tian W, Chen D. Promotion effect of cobalt doping on microwave-initiated plastic deconstruction for hydrogen production over iron catalysts. Appl Catal B Environ 2023;327:122451.
221. AlAreeqi, S., Ganley, C., Bahamon, D. *et al.* Rational design of optimal *bimetallic* and *trimetallic* nickel-based single-atom alloys for bio-oil upgrading to hydrogen. *Nat Commun* **16**, 2639 (2025).
222. *Chenyu Ding, Xiaomin Hu, Wenjing Sun, Reshalaiti Hailili, Fuxia Liao, Chenghong Shu, Jia Huang, Lihong Huang, and Ning Wang, Interface of Ni-$MgCr_2O_4$ Spinel Promotes the Autothermal Reforming of Acetic Acid through Accelerated Oxidation of Carbon-Containing Intermediate Species, ACS Catalysis* ***2023*** *13 (7), 4560-4574.*
223. Jin B, Wang K, Yu H, He X, Liang X. Engineering oxygen vacancy-rich CeO_x overcoating onto Ni/Al_2O_3 by atomic layer deposition for bi-reforming of methane. Chem Eng J 2023;459:141611.
224. Nascimento JP, Bezerra R de CF, Assaf EM, Lucredio AF, Araujo RS, Saraiva GD, et al. Investigation of the Deactivation Behavior of MeMo/La_2O_3-Al_2O_3- and MeMo/Nb_2O_5 Supported Catalysts (Me = Pt, Ni, and Co) in Tri-Reforming of Methane. Energy and Fuels 2022;37:3836–53.
225. Alshareef R, Nahil MA, Williams PT. Hydrogen Production by Three-Stage (i) Pyrolysis, (ii) Catalytic Steam Reforming, and (iii) Water Gas Shift Processing of Waste Plastic. Energy & Fuels 2023;37:3894–907.
226. Salah C, Cobo S, Pérez-Ramírez J, Guillén-Gosálbez G. Environmental Sustainability Assessment of Hydrogen from Waste Polymers. ACS Sustain Chem Eng 2023;11:3238–47.
227. Chari S, Sebastiani A, Paulillo A, Materazzi M. The Environmental Performance of Mixed Plastic Waste Gasification with Carbon Capture and Storage to Produce Hydrogen in the U.K. ACS Sustain Chem Eng 2023;11:3248–59.

228. Odenweller, A., Ueckerdt, F., Nemet, G. F., Jensterle, M., Luderer, G. Probabilistic feasibility space of scaling up green hydrogen supply. *Nat Energy* **7**, 854–865 (2022).
229. Brandt, J., Iversen, T., Eckert, C. *et al.* Cost and competitiveness of green hydrogen and the effects of the European Union regulatory framework. *Nat Energy* **9**, 703–713 (2024).
230. Wei, X., Sharma, S., Waeber, A. *et al.* Comparative life cycle analysis of electrolyzer technologies for hydrogen production: manufacturing and operations. *Joule* **8**, 3347-3372 (2024).
231. de Kleijne, K., Huijbregts, M.A.J., Knobloch, F. *et al.* Worldwide greenhouse gas emissions of green hydrogen production and transport. *Nat Energy* **9**, 1139–1152 (2024).
232. Spek, M., van der Banet, C., Bauer, C. *et al.* Perspective on the hydrogen economy as a pathway to reach net-zero CO_2 emissions in Europe. *Energy Environ Sci* **15,** 1034–1077 (2022).